(non-peer reviewed preprint)

Frictional Properties of Simulated Fault Gouges subject to Normal Stress Oscillation and Implications for Induced Seismicity

Bowen Yu[1], Jianye Chen[1*], Christopher J. Spiers[1,2], Shengli Ma[1], Miao Zhang[1], Wenbo Qi[1], and Hao Chen[1]

[1]State Key Laboratory of Earthquake Dynamics, Institute of Geology, China Earthquake Administration, Beijing, China.

[2]HPT Laboratory, Department of Earth Sciences, Utrecht University, Netherlands.

Corresponding author: Jianye Chen (jychen@ies.ac.cn)

Key Points:

- Fault weakening and unstable events can be readily triggered by normal stress oscillations when the gouge is slightly velocity-weakening.
- Fault resonance occurs at oscillation frequencies in the range 0.05–0.1 Hz.
- An extended microphysical model was built to quantify the mechanical behavior and tested using active ultrasonic technology.

Abstract

Under critical conditions where experimental fault slip exhibits self-sustained oscillation, effects of normal stress oscillation (NSO) on fault strength and stability remain poorly understood, as do potential effects of NSO on natural and induced seismicity. In this study, we employed double direct shear testing to investigate the frictional behavior of a synthetic, slightly velocity-weakening (SVW) fault gouge (characterized by self-sustained oscillation under quasi-static shear loading), when subjected to NSO at different amplitudes (5–20% of 5 MPa) and frequencies (0.001–1 Hz). During the experiment, fault displacement and gouge layer thickness were measured. Transmitted ultrasonic waves were also employed to probe grain contact states within the gouge layer. Our results show that fault weakening and unstable slip can be triggered at NSO frequencies ranging from 0.03 to 0.1 Hz and amplitudes exceeding 5%. Interestingly, an amplified shear stress drop and weakening effect were observed when the NSO frequency fell in 0.05–0.1Hz. Analysis of transmitted ultrasonic waves in tests on the SVW gouge revealed fault dilation, accompanied by unstable slip and weakening. By extending an existing microphysical model (the "CNS" model), to account for elastic effects of NSO on gouge microstructure and grain contact state, the mechanical and wave data obtained in our experiments on the SVW gouge was reproduced, suggesting an approach for modelling fault instability under upper crustal (SVW) conditions where normal stress is perturbed by subsurface operations, such as periodic gas storage stimulation of reservoir formations.

Plain Language Summary

To mitigate induced fault slip and seismicity associated with subsurface industrial activities that create oscillating stress, it is crucial to comprehend the effects of oscillation on fault friction. We used an experimental fault to mimic a potentially unstable fault at shallow depth and tested the effects of normal stress oscillation (NSO) on its shear strength. Various

amplitudes and frequencies of NSO were investigated. An active ultrasonic source was employed to probe the microstructure of the gouge layer. Our results suggest that unstable slip can be easily triggered by applying NSO. Fault weakening and shear stress fluctuations are amplified within a limited range of oscillation frequency. Increasing amplitude causes greater fault weakening and stress fluctuations. The transmitted ultrasonic waves are sensitive to the change in mechanical properties of fault zone, reflecting that fault dilation is the main mechanism associated with fault weakening and instability. We present a microphysical model that reproduces and explains the mechanical and ultrasonic results, offering a potential route to extrapolate laboratory data to field conditions in the future.

1 Introduction

Recent studies have revealed that induced seismicity is caused by changes in stress field associated with industrial operations such as natural gas production (Candela et al., 2019), CO2 storage (Verdon, 2014), wastewater injection (Amemoutou et al., 2021; Keranen et al., 2013), hydraulic fracturing (Cao et al., 2022), water reservoir impoundment (Gupta, 2002) and geothermal development (Cacace et al., 2021; Ellsworth et al., 2019) – many of which involve repeated or even periodic activity. Apart from induced seismicity, stress perturbations and slip on faults also generate engineering risks, such as leakage from faulted reservoir systems (Glubokovskikh et al., 2022) and deformed wellbore casings (Chen et al., 2017; Zhang et al., 2022), leading to substantial financial consequences (Langenbruch et al., 2020). Natural processes can also alter the stress distribution on faults, ultimately influencing seismic activity within a given region. For example, large earthquakes alter the stress state in the vicinity of the main fault (Harris, 1998) but also more remotely, through dynamic stressing and triggering by seismic waves (Hill et al., 1993). Moreover, Earth and ocean tides can modulate seismic cycles by generating periodic stress perturbations on faults (Heaton, 1975; Schuster, 1997). Physical and chemical processes that take place during coseismic and interseismic periods (such as frictional heating, thermal pressurization, dehydration of clay minerals, and fault dilation/compaction/healing) may also affect the slip behavior of faults by changing the pore pressure distribution within the fault zone (Rice, 2006; Sleep & Blanpied, 1994; Yu et al., 2023). Therefore, in the framework of identifying and mitigating both induced and natural seismic hazards, it is necessary to unveil the physical mechanisms that control the effects of stress perturbation on fault mechanical behavior and to establish a constitutive model to quantify these effects.

Previous experimental fault friction studies have demonstrated two distinct evolutions of fault strength when the sample is subjected to a normal stress step (an analog to dynamic stress change). The first type suggests a two-stage evolution, in which shear strength changes along an elastic path followed by a time-dependent transient evolution (Hong & Marone, 2005; Linker & Dieterich, 1992). These authors conducted experiments using bare surfaces of Westerly Granite at reference normal stress of 5 MPa at room temperature and room humidity. Hong and Marone (2005) found similar evolution in tests on quartz and quartz-smectite gouges at room temperature, using applied normal stresses ranging from 10 to 45 MPa. Effects of humidity were also investigated in their study, which showed that increasing humidity can cause an increase in transient shear stress response for pure quartz but a decrease for quartz-smectite gouge. The second type of evolution consists of a single-stage transient response approaching a new steady-state level, as reported by Prakash(1998), who investigated hard metal (4340VAR structural steel, titanium alloy and tungsten based tool cermet) friction at room temperature and humidity, but at much higher applied loading rates (1–30 m/s) and normal stresses (500 MPa–3 GPa). The differences might be due to the differences in machine stiffness adopted in these studies (Shreedharan et al., 2019).

In experiments in which normal stress oscillates sinusoidally, Pignalberi et al. (2024) found that large amplitude, short-period oscillation caused reduction of fault strength when using quartz as simulated gouge. Boettcher and Marone (2004) made similar experimental observations for quartz gouge. They also found a critical normal vibration frequency at which shear stress oscillations are amplified significantly and a maximum phase lag is achieved. This behavior is similar to the fault resonance obtained in the numerical research of Perfettini et al. (2001), where variations in shear strength and slip velocity were strongly enhanced at specific vibration frequencies. However, such resonance can only occur when the following 3 conditions are achieved:

1) The shear stiffness of the loading system k is close to the critical value k_c (Rice & Ruina, 1983), given by:

$$k_c = \sigma_n^{eff}(b-a)/D_c \tag{1}$$

where σ_n^{eff} is the effective normal stress, a and b are constitutive parameters used to describe the direct effect and evolution effect when a fault is subjected to a velocity step, and D_c is the characteristic displacement over which fault friction evolves to a new steady state.

2) The oscillation period is close to the critical period $T_{critical}$ (Rice & Ruina, 1983):

$$T_{critical} = 2\pi\sqrt{\frac{a}{b-a}\left(\frac{D_c}{V}\right)} \tag{2}$$

where V refers to the fault shearing velocity.

3) The critical oscillation amplitude ϵ_c must be exceeded (Perfettini et al., 2001):

$$\epsilon_c \approx \frac{b-a}{\mu_{ss}} \frac{1-\frac{k_c}{k}}{\sqrt{1+\left(1-\frac{\alpha}{\mu_{ss}}\right)^2 \frac{(b-a)}{a}}} \tag{3}$$

where μ_{ss} is the steady-state friction coefficient, α is a parameter used to describe the evolution of state following a change of normal stress in the extended rate-and-state friction law (Linker and Dieterich, 1992); see more details regarding this model below. Sinusoidal (confining) stress oscillation has also been found to modulate the distribution of (micro)seismicity produced by experimental "saw-cut" faults in triaxial compression tests (Colledge et al., 2023). These authors reported that the response amplitude of the acoustic emission event distribution increased with increasing confinement oscillation amplitude, period and imposed velocity. Moreover, the Gutenberg-Richter b-value (Gutenberg & Richter, 1944) showed a sinusoidal evolution when using the largest oscillation amplitude.

Compared with the experiments mentioned above, where normal stress was varied at zero or constant pore pressure, pore fluid pressure oscillation experiments are more directly relevant to injection-induced seismicity. Using saw-cut sandstone cylinders as the simulated fault, Noël et al. (2019) showed that larger amplitude pore fluid oscillations facilitated unstable fault slip. Compared with continuous injection, oscillation of the pore fluid pressure can lower the maximum moment magnitude of induced laboratory earthquakes (Zhu et al., 2021). One general observation, mainly in triaxial tests on porous rock samples, is that pore pressure oscillation can reduce rock strength, resulting in early brittle failure of the sample (Farquharson et al., 2016; Noël et al., 2019). Surges in acoustic events correspond to the fluid pressure maxima, as observed by Farquharson et al. (2016) and Noël et al. (2019), while Chanard et al. (2019) reported the opposite trend.

Slide-hold-slide experiments, frequently used to assess frictional healing progress, indicate a further effect connected to regular stress oscillation. In particular, continuous normal stress oscillation (NSO) enhances stress relaxation during hold periods and speeds up the frictional healing process in quartz gouge (Richardson & Marone, 1999). In addition, when a fault initially exhibits regular stick slips at constant axial loading rate in a triaxial saw-cut test (i.e. when the system stiffness $k < k_c$), the degree of correlation between the timing of these simulated earthquakes and a given phase of applied stress oscillation (applied by varying the axial loading rate) increases with the oscillation amplitude (Lockner and Beeler, 1999). Cochard et al. (2003) have further shown that extremely high NSO frequency, compared with the time interval of stick-slip, can stabilize stick-slip.

To simulate the evolution of the fault shear stress after a normal stress step, Kilgore et al., (2017) build a theoretical model based on the change of contact area. However, most theoretical work was performed based on the classical RSF law. Effects of variable normal stress were not considered when the RSF friction law was first proposed (Dieterich, 1979; Ruina, 1983). To account for the coupling between normal stress and shear stress changes during slip on an inclined fault, Chambon and Rudnicki (2001) combined the original RSF law with an extended spring-slider model to simulate the dynamics of fault motion in an elastic rock mass. Linker and Dieterich (1992) extended the RSF model itself (to a form hereafter referred to as the "LD92 model") by introducing a newly defined parameter α, which was used to describe the sudden change in the state variable θ when a fault is subjected to a step change in normal stress. Dieterich and Linker (1992) then used the LD92 model to derive the critical stiffness in the context of variable normal stress. Subsequent experimental results have been effectively replicated by this model (Hong & Marone, 2005; Shreedharan et al., 2019). However, there are some shortcomings. For example, when normal stress increases and then decreases, LD92 model cannot predict the asymmetric behavior of shear stress observed (Hong & Marone, 2005). Fault-healing behavior is also not fully reproduced (Richardson & Marone, 1999). Bureau et al. (2000)

identified the lack of consideration of gouge elasticity as the cause of these contradictions. They discovered that neither the LD92 model nor the RSF models could adequately explain the response of shear strength in samples subjected to high-frequency normal stress oscillation. More recently, Chen and Spiers (2016); Niemeijer and Spiers (2007) have proposed an alternative, microphysically-based model (known as the "CNS model"), which has already been successfully applied to fit and explain steady-state and transient fault friction (Chen & Spiers, 2016; Niemeijer & Spiers, 2007). All of the parameters in the classical RSF law have their equivalent expressions in the CNS model (Chen et al., 2017). An intrinsic advantage of this model is that effects of normal stress on friction are explicitly allowed for through their influence on deformation by both intergranular sliding and creep at the grain scale. Therefore, the CNS model has the potential to predict frictional behavior under variable normal stress, although elasticity of the fault gouge is not considered in the current form of this model.

Some of the above experimental studies on the effects of variable normal stress were performed under room temperature conditions at which the fault gouge used was characterized by velocity-strengthening behavior, while others mainly focused on stick slip reflecting velocity weakening. However, at a depth of 1–5 km where most induced seismicity occurs (Lei et al., 2019; Yang et al., 2020), slightly velocity-weakening (SVW) behavior is also possible and even expected (Boatwright & Cocco, 1996; Carpenter et al., 2016). This means that an unstable fault segment might lie in the transition zone between the velocity-weakening and velocity-strengthening regimes, where slip is characterized by "self-sustained oscillation", that is a mechanical behavior showing episodic stable sliding under quasi-static loading (Baumberger et al., 1999). To our knowledge, the effects of variable normal stress on the frictional behaviors of

SVW fault gouges are still not well understood, yet may be of special importance for induced seismicity.

Against this background, the present paper has two aims. The first is to explore the little-known effects of oscillating normal stress on the frictional behavior of SVW fault gouges. Given that the LD92 model cannot reproduce the full spectrum of fault slip behavior seen under variable normal stress, our second purpose is to attempt to quantify and explain the effects of oscillating normal stress on shear strength using the CNS model. We used a double-direct-shear (DDS) configuration to study the influence of normal stress oscillation (NSO) on fault stability. A specially chosen synthetic gouge with SVW frictional properties was used as a “model” or simulated fault gouge to fill the experimental faults, aiming at generating self-sustained oscillation behavior under quasi-stationary loading conditions. Additional sinusoidal loading with different amplitude and frequency was superposed on the background normal stress to apply NSO to the fault. Fault displacement and thickness change were monitored continuously using an LVDT and high-resolution eddy current sensors, respectively. In addition, an active ultrasonic source was employed to probe the grain contact state within the gouge layer (Nagata et al., 2014). We also performed one control experiment on chlorite gouge so that the results of a velocity-strengthening (VS) material could be compared with those using SVW gouge. In addition, we extend the current form of the CNS model by introducing terms describing gouge elasticity as well as the stress coupling between the gouge layer and the surrounding medium. We test this modified model by comparing it with our mechanical data and with the grain contact state examined using transmitted ultrasonic waves.

2 Materials and Methods

2.1 Sample Materials and Configuration

The experiments presented in this study were conducted using a horizontal, biaxial loading machine at the Institute of Geology, China Earthquake Administration, Beijing (Fig. 1a). The sample assembly had a double direct-shear (DDS) configuration wherein two layers of simulated fault gouge were sandwiched between three granite blocks (Fig. 1b). The size of the middle and side blocks was 100×50×50 cm and 200×50×50 cm, respectively. Each of the four sliding surfaces was roughed using 60# abrasive paper. The starting thickness of the gouge layer was 700 μm. A special, commercially provided mineral mixture was used to represent slightly velocity-weakening fault gouges (the SVW gouge mentioned in the Introduction and referred to as such henceforth). XRD analysis revealed that the SVW gouge contains 39.19 wt% dolomite, 31.24 wt% bassanite, 22.74 wt% calcite, and 6.83 wt% quartz (Fig. S1). We used this material because self-sustained oscillation behavior can emerge during quasi-static loading (Fig. S2). The SVW gouge was crushed and sieved using 250# and 300# sieves, so that the grain size could be controlled between 48 μm and 58 μm. We also conducted one control experiment on velocity-strengthening chlorite gouge (hereafter refer to as the "VS gouge"), aiming at testing if the SVW gouges (which tend to show spontaneous instability during quasi-static loading) respond differently to NSO compared with VS gouges. The chlorite samples were the same as used by Yu et al. (2023) and contained more than 96 wt% chlorite. We sieved the chlorite samples with a 200# sieve so that the grain size was smaller than 75 μm.

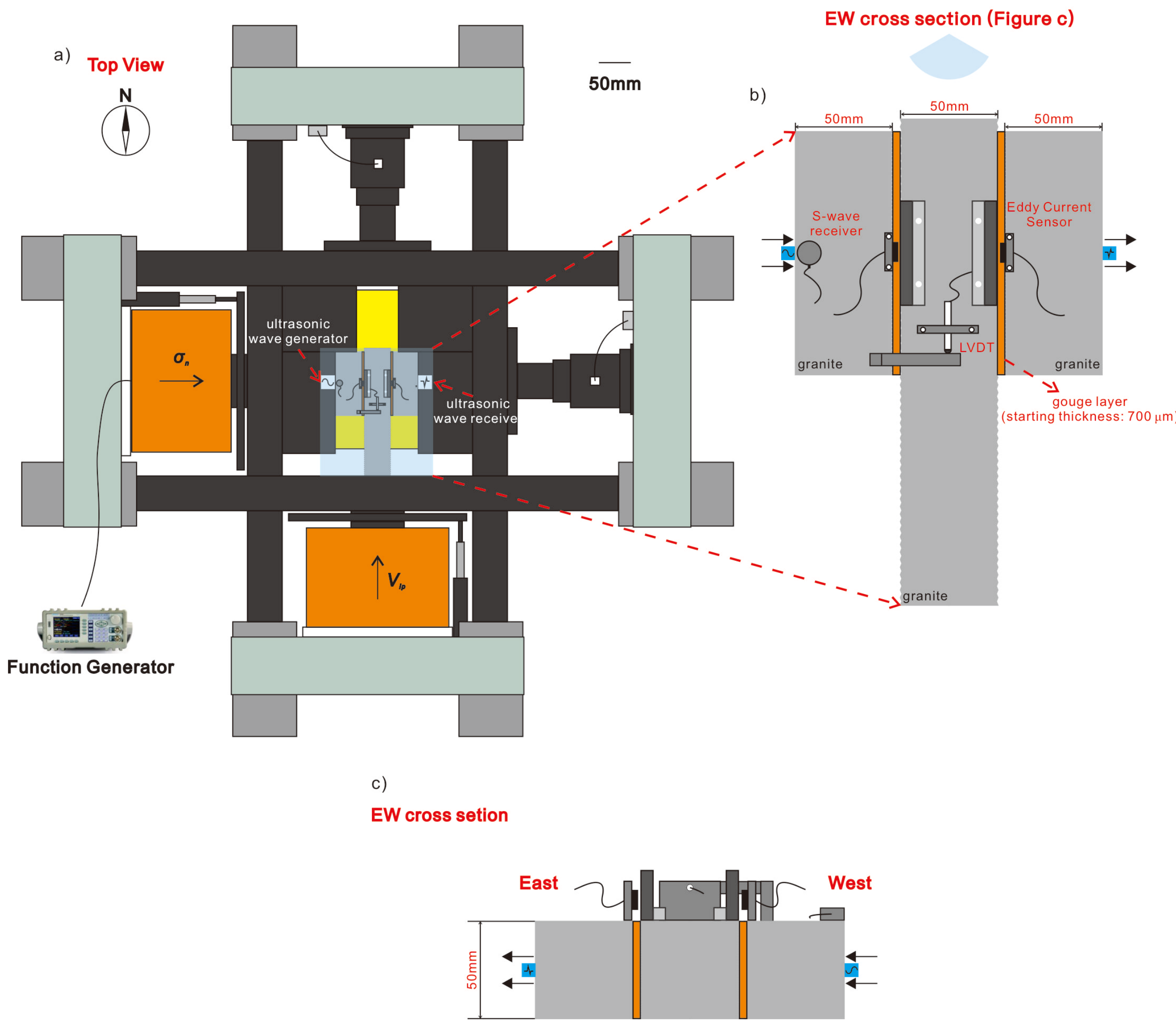

Figure 1. a) Top view of the machine and sample assembly used in this study. b) Enlarged figure of the sample and set-up of sensors. c) EW cross section of the sample assembly.

On the top surface of the sample, we installed two high-resolution eddy current sensors (MICRO-EPSILON eddyNCDT 3060, with a resolution better than 0.02 μm and measuring range of 1 mm) and one LVDT (PETER HIRT GmbH T500 Serie) to measure the thickness change of gouge layer and displacement along fault (Fig. 1b and 1c). Another two LVDTs, installed between the loading plate and machine framework, were used to measure the displacement of the two servo-control loading rams. The data acquisition frequency for the stress, fault thickness and sliding displacement was 1 kHz. We also implemented an active ultrasonic source to monitor the state of grain contacts within the gouge layers. Two P-wave piezoelectric ceramics ultrasonic transducers were attached with a film of ultrasonic couplant on opposite sides of the sample assembly. One (Olympus V112-RM) was used to provide the active ultrasonic source, which was characterized by a sinusoidal pulse with a frequency of 0.1 MHz and an amplitude of 400 mV. The pulse rate is around 240 Hz after superposition. The second (Softland RS-15A) was linked to a 3 MHz data acquisition system to receive the transmitted ultrasonic waves. Due to the significant difference in voltage between the excitation and data recording system, we cannot record the actual waveform of the excitation pulse during experiments. Instead, we installed an S-wave transducer on the top surface of the sample assembly, close to the active ultrasonic source, in an attempt to approximate the excitation time of each pulse. We did not employ an active ultrasonic source in the chlorite control experiment, due to some technical issues.

2.2 Experimental Procedures

We performed one NSO experiment (HBR-22-56, Table 1) on SVW gouge as well as one control NSO experiment (HBR-21-67, Table1) on VS gouge. Both experiments were performed at room temperature and humidity (~30% from the lab room humidity measurement). After mounting the sample assembly into the loading framework, we first performed normal load cycling pre-tests without shearing the sample (background normal stress of 5 MPa while the oscillation amplitude and frequency were 20% and 0.1 Hz, respectively) on the sample, aiming at measuring the compression modulus of the gouge material (Fig. S3) and at testing the sensitivity of received acoustic waves to the normal stress variation. We removed the normal stress after this pre-test and recorded the data obtained separately. Subsequently, we started the procedure of the NSO experiment. A full experimental curve is provided in Fig. S4. Normal stress on the simulated faults was first increased to 7 MPa under servo control and then a constant load-point velocity of 0.25 μm/s was imposed to advance the middle granite block. We first sheared the gouge layers through around 600 μm to obtain a constant steady state friction coefficient. A load-unload test was performed when the fault slip displacement approached its target value (600 μm). After this pre-slip stage, we controlled the driving ram, at load point, to move backwards under constant velocity control (0.25 μm/s) until around 50% reduction of shear stress was achieved. The purpose of this was to reduce the shear stress on the fault to a value below the shear strength at 5 MPa normal stress, thus avoiding a jump or onrush of the central block when reducing the normal stress to 5 MPa. Subsequently, normal stress was decreased to 5 MPa and excitation of the active ultrasonic source commenced. To produce oscillations in normal stress, we used a function generator linked to the servosystem controlling the normal loading ram. Two types of normal stress oscillation (NSO) were investigated in single experiment, on both the SVW gouge and the VS gouge (see Table 1). In one type of NSO (Type I), the frequency ranged from 0.001 to 1 Hz while the amplitude was 20% (for SVW gouge) and 5% (for VS gouge) of background normal stress. In the other (Type II), the NSO amplitude was varied in the range of 5–20% of the background normal stress while the oscillation frequency was kept constant at 0.6 (for SVW gouge) and 0.3 Hz (for VS gouge). During both experiments, we employed the Type I NSO first and then Type II. After imposing the desired types of NSO, we halted the experiment, removed the shear stress and then the normal stress from the sample assembly and finally collected fragments of deformed gouge for microstructural analysis. Note that any effect of shearing displacement on the velocity dependence of our gouge samples is expected to be negligible because the total shearing displacement (~ 3mm) applied in our experiments was significantly smaller than the displacement threshold (4–10 mm) for transitions in velocity dependence reported in previous studies (Beeler et al., 1996; Hadizadeh et al., 2015; Noël et al., 2023).

Table 1. Experimental parameters. V_{lp} is the load-point velocity. σ_n is the background normal stress. A is the normal stress oscillation amplitude, which is the percentage of σ_n. f is the oscillation frequency. Type I and Type II NSO refer to two different types of NSO in each experiment, including 1) NSO with different frequencies while amplitude is constant, and 2) NSO with different amplitudes while frequency is constant. In both experiments, we employed the Type I NSO first and then the Type II NSO.

Experiment ID	Material	V_{lp}, µm/s	σ_n, MPa	Type I NSO		Type II NSO		Ultrasonic source
				A, %	f, Hz	A, %	f, Hz	
HBR-22-56	SVW gouge	0.25	5	20	0.001–1	5–20	0.6	Employed
HBR-21-67 (Control experiment)	VS gouge	0.5	10	5	0.001–1	5–20	0.3	Not employed

2.3 Data processing and analysis

2.3.1 Mechanical data treatment

In this study, we determined shear stress and normal stress acting on the two gouge sample layers, in each experiment, simply by dividing the applied shear and normal forces by sample surface area, thus obtaining sample scale averages. Shear displacement was obtained from the LVDT located on the central granite block. As the local distortion of the sample assembly did not have significant impact on the instantaneous response of shear displacement (Fig. S5), we did not apply any stiffness correction to this data. Changes in fault gouge thickness were calculated by taking the average displacement recorded by the eddy current sensors bridging each fault zone.

2.3.2 Ultrasonic data analysis

The active ultrasonic P-wave source implemented in this study aimed at examining real-time changes in samples stiffness and thus inferring changes in contact area (Nagata et al., 2014). The data in Fig. 2a represents a typical signal corresponding to the transmitted P-wave alongside that recorded by the S-wave sensor, which can be used to indicate the excitation time of each pulse. The transmission coefficient T, wave velocity $V_{p,}$ and coda wave correlation coefficient C, measured between the received waveform and a predefined wave template, are three key parameters that can be derived from the dataset. Calculation of the transmission coefficient T follows from the general expression applied to ultrasonic waves transmitted through two experimental fault surfaces (Nagata et al., 2012; Shreedharan et al., 2019):

$$T = \sqrt{\frac{A_T}{A_0}} \tag{4}$$

Here A_T is the peak-to-peak amplitude (difference between maximum and minimum amplitude) measured in the first 100 μs after arrival (see red-highlighted portion of received wave in the enlarged figure of Fig. 2a). A_0 refers to the value obtained in the case that the ultrasonic wave transmits through a single, intact granite block only. In this study, we normalized the T value obtained after NSO against T before NSO to investigate the variations of contact state caused by NSO.

P-wave velocity V_p is defined as the travel distance (0.15 m, which is the total width of 3 forcing blocks. The total width of 2 gouge layers is not considered.) divided by the difference in arrival time between the received wave and the so-called “incident” wave received by the S-wave transducer. Although this is not the absolute wave velocity of the whole DDS assembly, variations due to vibrations in normal stress can still be captured. Normal stress oscillation is expected to lead to a phase-shift of the coda wave (defined here as the portion of signal between

3437 μs and 3778 μs, measured from the excitation time) compared to the wave template obtained during constant normal stress conditions (Fig. 2b). Based on this fact, we calculated the temporal evolution of the correlation coefficient *C* between the coda waves of the signal received during NSO and a wave template selected from the quasi-static loading stage, using the formula for Pearson's correlation coefficient (Pearson & Galton, 1997).

To estimate the evolution of contact state during NSO, the elastic component of *T*, V_p and *C* should be subtracted. This was achieved via the following steps: 1) determine a linear fitting function between applied normal stress and the recorded ultrasonic parameters (Fig. S6). The slope of the linear fit represents the elastic component of the corresponding ultrasonic parameter caused by unit change of normal stress. Note that the dataset used for the linear fit was derived from the experiment conducted at high oscillation frequency (1 Hz in this study), because the phase lag of mechanical response compared with the applied normal stress is negligible in this case. 2) By subtracting the product of the slope and the variation of normal stress from the original recording of *T*, V_p, and *C*, we can determine an evolution of the ultrasonic parameters without the elastic component. We did not correct V_p because it is insensible to the fault unstable events due to the low sampling rate.

According to previous research(Beeler et al., 2010; Nagata et al., 2008; Shreedharan et al., 2019), we expect that the three parameters listed above (i.e., *T*, V_p and *C*) will be directly proportional to the mean grain contact area (i.e., contact state or stiffness) so that the gouge microstructure underlying its macroscopic mechanical behavior during NSO could be probed (Fig. 2c).

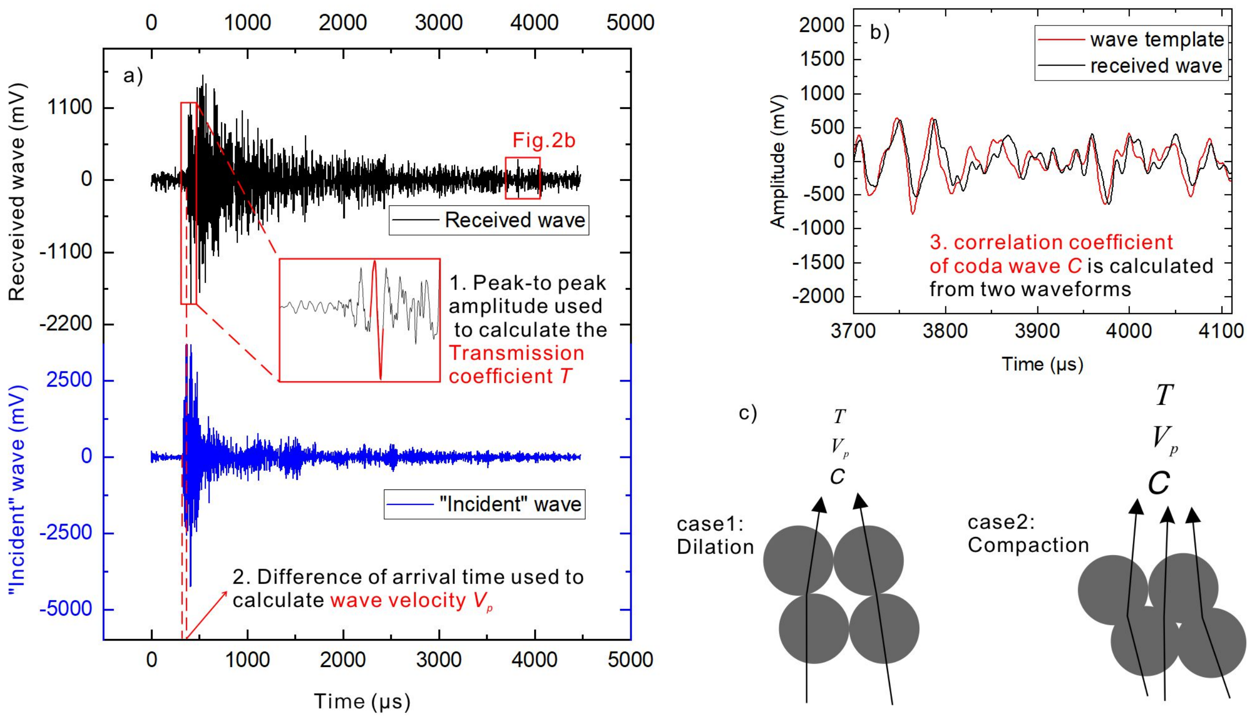

Figure 2. Analytical methods applied to the transmitted ultrasonic waves. (a) Peak-to-peak amplitude used to calculate transmission coefficient *T*. Travel time is calculated from the difference of arrival time between the received waveform and the "incident" waveform as recorded by the S-wave sensor. The wave velocity V_p is defined as the width of whole DDS assembly (0.15 m, total width of 2 gouge layers is ignored) divided by the travel time. (b) Phase shift of the coda wave recorded during NSO compared with the coda wave template that is obtained during quasi-static loading, indicating the change of grain contact state. The correlation coefficient *C* was calculated between the coda wave of the received waveforms during NSO and that of the wave template. (c) A schematic that shows the influence of grain contact state (i.e., contact area or stiffness) on the response of transmitted ultrasonic waves. *T*, V_p, and *C* are expected to increase with increasing fault compaction. Note here that both of creep processes (inelastic) and elastic deformation can change the contact state and hence the elastic wave propagation behavior.

3 Results

In this section, we first present the results of our NSO experiments on the SVW gouge, including the effect of oscillation frequency and amplitude on the stability of our simulated fault zones (see experiment HBR-22-56 in Table 1), showing data on the response of shear stress, fault thickness change and displacement. We then present typical results for ultrasonic parameters. Experimental results (shear stress, fault thickness and displacement) obtained for the VS gouge (HBR-21-67, Table 1) are also presented for comparison.

3.1 Experimental results for the SVW gouge

3.1.1 Effects of Oscillation Frequency and Amplitude on Fault Slip Behavior

The results of the NSO experiment performed on the SVW gouge with varying oscillation frequencies (the first test sequence of HBR-22-56) are shown in Fig. 3. The background normal stress was 5 MPa and the oscillation amplitude was kept constant at 20% while the oscillation frequency ranged from 0.001 to 1 Hz (refer Table 1). The response of the driving ram reached its limit when vibrating rapidly, which is why the amplitude of normal stress is slightly smaller at higher frequency than at lower frequency (Fig. 3a). The shear stress supported by the experimental faults reaches a plateau at 4.2 MPa at constant σ_n, then abruptly decreases to 3.6 MPa due to the onset of NSO at 1 Hz (Fig. 3b), accompanied by fault dilation (Fig. 3c, 3d-3f). The average shear strength then recovers after a small displacement, reaching a relatively low, steady level compared with that under quasi-static loading, which indicates fault weakening. Similar levels of shear strength persist up to an NSO frequency of 0.03 Hz. At intermediate oscillation frequency (0.03–0.1 Hz), we can observe that some unstable events (a sudden and significantly large (i.e., resolvable from background) shear stress drop compared with the general level of shear stress reduction that occurs within one period of the imposed sine waveform) are triggered spontaneously within each period of fixed frequency. These unstable events occur consistently with decreasing normal stress and are always accompanied by fault dilation as well as acceleration (Figs. 3c, 3g-3i). Additionally, both fault weakening and the amplitude of shear stress oscillation become more significant. When we further decrease the oscillation frequency (0.01 Hz), unstable events disappear. Following termination of NSO, the average shear strength returns to its initial, pre-oscillation value. The average fault thickness change exhibits a gradual decrease during NSO and keeps decreasing after the cessation of NSO. This probably resulted from the extrusion or densification of the fault gouge (Kaproth & Marone, 2014; Scott et al., 1994) but we did not correct the thickness data regarding this effect. Therefore, only local variations of fault thickness are due to NSO.

The results of the NSO experiment on the SVW gouge with different oscillation amplitudes (the second test sequence of HBR-22-56) can be found in Fig. 4. The amplitudes of σ_n implemented here are 20%, 15%, 10% and 5% of the background value, while the background σ_n and frequency were kept constant at 5 MPa and 0.6 Hz (Fig. 4a). Again, we observe an instantaneous shear stress drop and accompanying dilation, as well as an acceleration of fault motion, after imposing NSO (Figs. 4b-4c). The data in Fig. 4 clearly show that increasing oscillation amplitude results in a larger fault weakening effect. At an amplitude of 20%, 15%, and 10%, unstable events are consistently triggered by NSO. Similarly, these unstable events occur consistently with decreasing normal stress and are always accompanied by fault dilation as well as acceleration (Figs. 4c, 4d-4f). The stress drop associated with each event increases with oscillation amplitude. At an amplitude of 5%, no unstable events are triggered and the response of shear stress is similar to that under constant normal stress, before NSO, which is characterized by self-sustained oscillation. This behavior is also restored, at the same mean shear stress level, after cessation of NSO. Background fault thickness gradually decreases throughout NSO, probably due to gouge extrusion or densification (Scott et al., 1994).

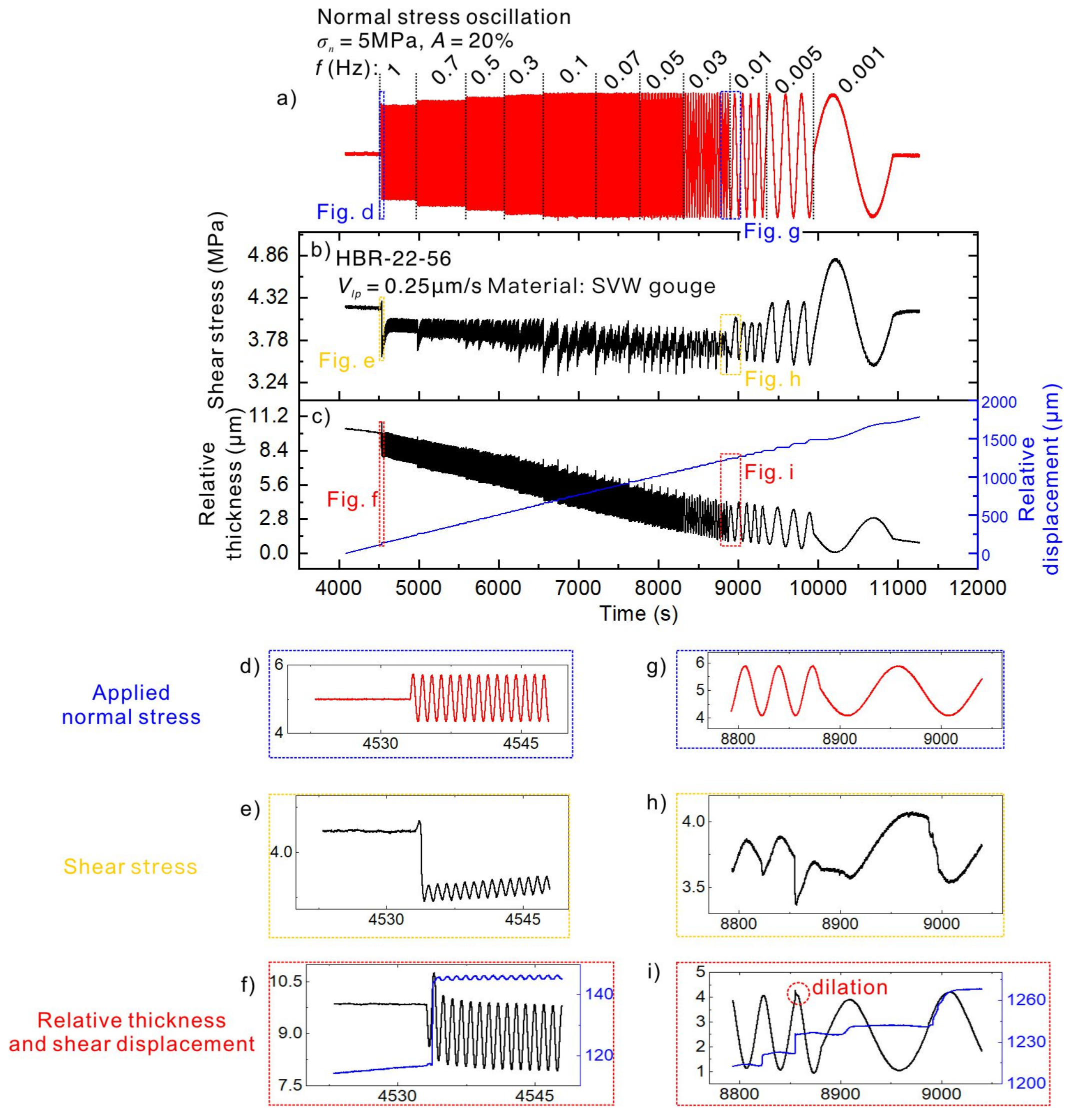

Figure 3. SVW gouge. Effects of oscillation frequencies on fault shear strength and thickness. The oscillation amplitude was kept constant at 20%. (a) Applied normal stress (b) Evolution of shear stress. (c) Fault displacement and thickness change of gouge layer. Continuous decrease of the background fault thickness is probably due to extrusion of gouge material. (d), (e), and (f) show enlarged curve segments for the highest NSO frequency. (g), (h), and (i) show enlarged curve segments that include an unstable event.

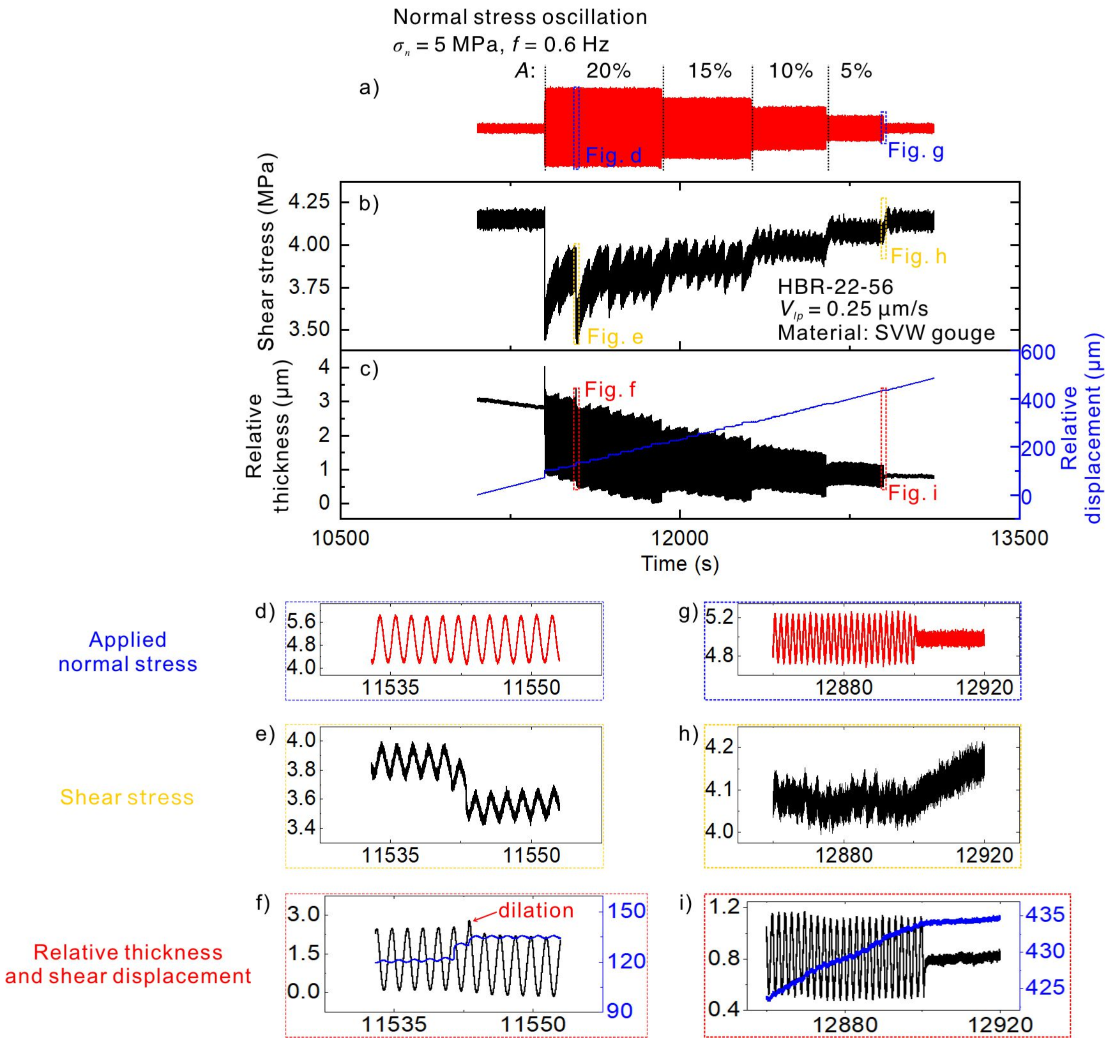

Figure 4. SVW gouge. Effects of oscillation amplitudes on fault shear strength and thickness. Oscillation frequency is 0.6 Hz. (a) Applied normal stress (b) Evolution of shear stress (c) Fault displacement and thickness change of simulated gouge layer. (d), (e), and (f) show enlarged curve segments that include an unstable event. (g), (h), and (i) show enlarged curves segments for the lowest NSO amplitude.

3.1.2 Response of Transmitted Ultrasonic Waves to NSO

Fig. 5 depicts how the transmitted ultrasonic waves respond to high-frequency NSO in the case of the SVW gouge. The figure compares how the transmission coefficient T, wave velocity V_p, coda wave correlation coefficient C and shear stress evolve after initiating NSO.

These data come from the experiment conducted at a frequency of 1 Hz and amplitude 20% (Experiment HBR-22-56, Table 1). *T* and *C* that were corrected to remove the elastic effect are also displayed together with the original data recorded (Figs. 5c and 5e). At the beginning of NSO, an instantaneous drop can be observed in *T*, V_p and *C*, alongside the drop in shear stress. *T* and *C* then decrease and increase respectively, while there is no evolution stage in V_p. Background changes of the three parameters evolve sinusoidally with oscillation of the applied normal stress. As the average shear stress increases to become stable, the average *T*, V_p and *C* become lower than the pre-NSO level, which, according to previous work (Gheibi & Hedayat, 2020; Shreedharan et al., 2020, 2021), implies a decrease in average grain contact area or stiffness after the oscillation phase. In other words, fault dilation occurs instantaneously at the onset of NSO and continues in the following stage.

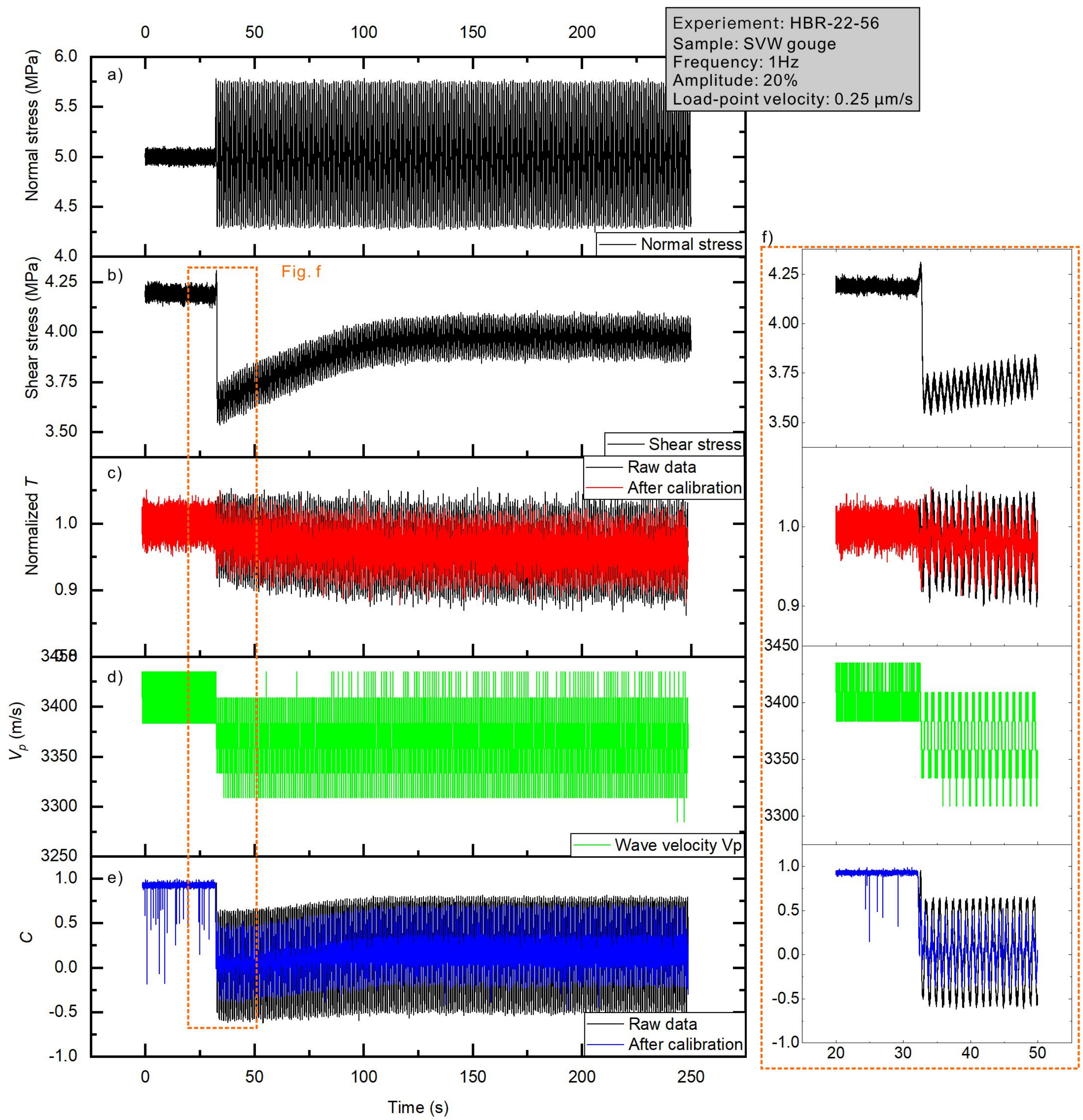

Figure 5. SVW gouge. Behavior of received ultrasonic wave to high-frequency NSO (1Hz). Although the oscillation amplitude was set as 20% of the mean normal stress, the real amplitude was around 15% because the loading ram could not move in a full stroke at high frequency (1 Hz). (a) Applied normal stress and the corresponding evolution of shear stress (b). The evolution of transmission coefficient *T* wave velocity V_p, and coda wave correlation coefficient *C* are shown in (c), (d), and (e) respectively. Calibrated *T* and *C* are also

displayed in (c) and (e) to remove the elastic effect. (f) shows enlarged curve segments for the data indicated by the orange rectangle in Figure. (b)-(e).

To explore the behavior of transmitted ultrasonic waves associated with unstable slip events triggered by medium-frequency NSO (refer Figs. 3 and 4), we examine the results of experiment HBR-22-56 on SVW gouge (Table 1), specifically during NSO at a frequency of 0.07 Hz and with amplitude 5% (Fig. 6). Transmitted coefficient *T*, wave velocity V_p and coda wave correlation coefficient *C* vary sinusoidally along with the normal stress in general. Two unstable events can be observed in Fig. 6b, featuring stress drops of 0.06 MPa and 0.24 MPa. No instantaneous changes accompany the smaller event. However, sudden drops in *T* and *C* occur in association with the larger event, indicating fault dilation, while wave velocity is not affected within measurement resolution (Figs. 6c-6d). The average value of *C* remains relatively low after this event, whereas *T* increases to slightly higher mean levels.

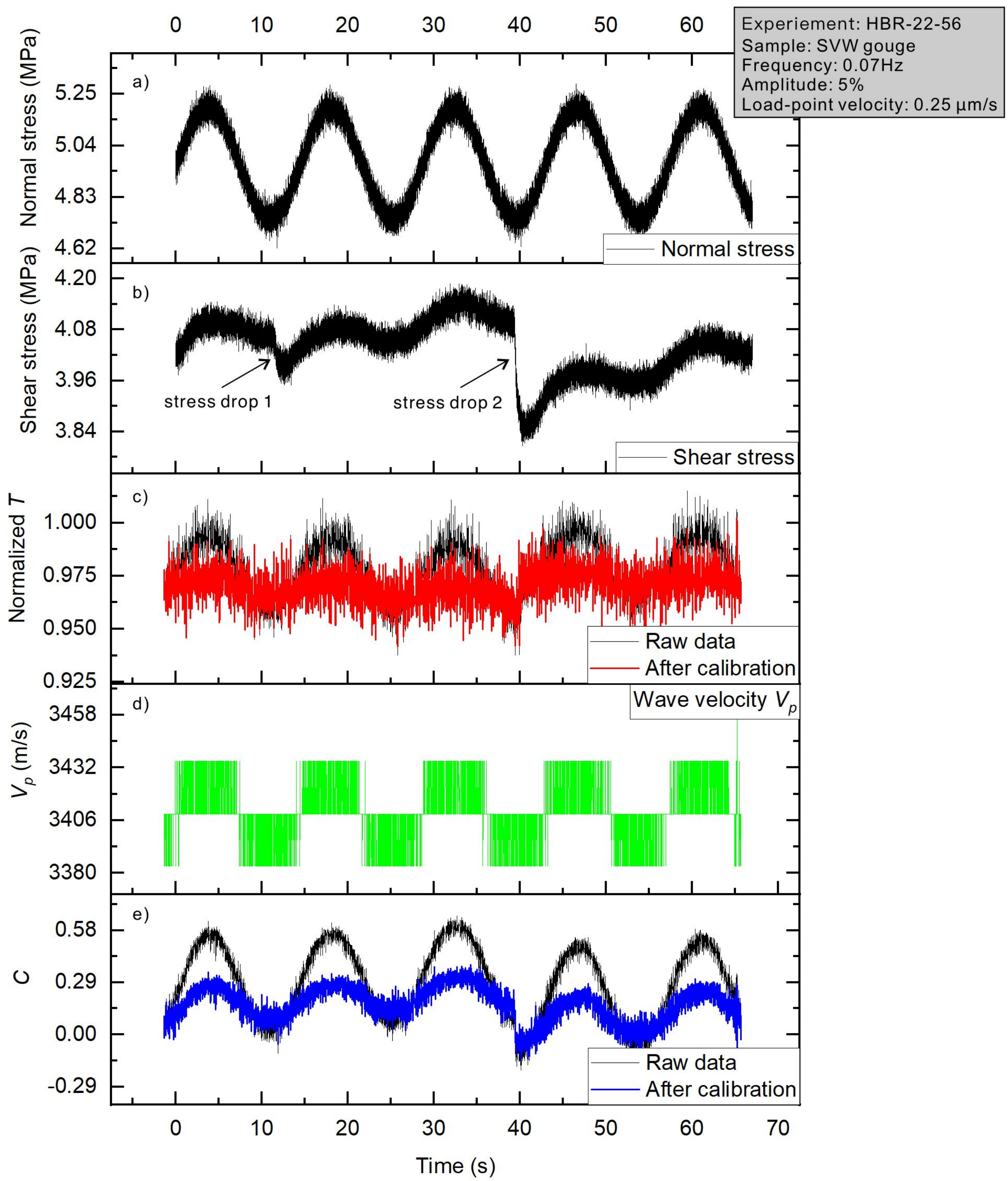

Figure 6. SVW gouge. Behavior of received ultrasonic waves during intermediate-frequency NSO (0.07 Hz). Oscillation amplitude is 5%. (a) Applied normal stress and the corresponding evolution of shear stress (b). Evolution of transmission coefficient *T*, wave

velocity V_p, and coda wave correlation coefficient C are shown in (c), (d), and (e) respectively. Corrected *T* and *C* are also displayed in (c) and (e) to remove the elastic effect.

3.2 Experimental results for the VS gouge

To compare the results of our SVW material with that of a VS material, we performed NSO experiments on pure chlorite gouge (HBR-21-67, Table 1). Fig. 7 displays the results of the NSO experiment conducted with different oscillation frequencies. An instantaneous drop in shear stress occurs at the onset of NSO (Fig. 7b). At NSO frequencies ranging from 1 to 0.05 Hz, shear stress shows a near sawtooth-shaped waveform, and exhibits small superimposed fluctuations, but there are no unstable events triggered. When we further decrease the oscillation frequency towards 0.001 Hz, shear stress and normal stress evolve simultaneously. Fault thickness evolves sinusoidally with normal stress (Figs. 7c and 7d). Continuous compaction can be observed especially after the 0.3 Hz oscillations, which might be caused by extrusion of simulated gouge or alignment of chlorite mineral. There are no sudden changes suggested by the fault displacement, implying that fault slip is stable in this case.

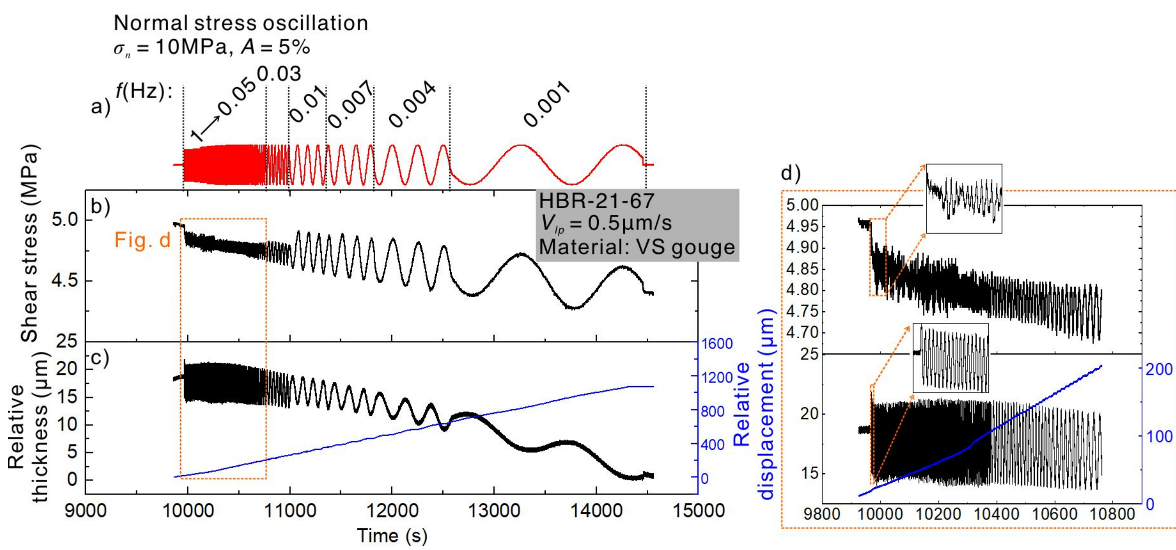

Figure 7. VS gouge. Result of NSO experiment performed with different oscillation frequencies for chlorite gouge. Background normal stress is 10 MPa. Oscillation amplitude

is 5% while frequency ranges from 1 to 0.001 Hz. The red curve in (a) denotes applied normal stress and (b) shows the shear stress. (c) Fault displacement and thickness change. d) shows the enlarged curve segment of the high-frequency data.

Fig. 8 shows the results of our NSO experiment performed under different oscillation amplitudes when using VS chlorite. Fault weakening increases with oscillation amplitude (Fig. 8b). However, NSO did not trigger any unstable events during the experiment even at the largest oscillation amplitude (20%). We did not observe any dilation of the fault gouge layer excepted at the start of the NSO experiment.

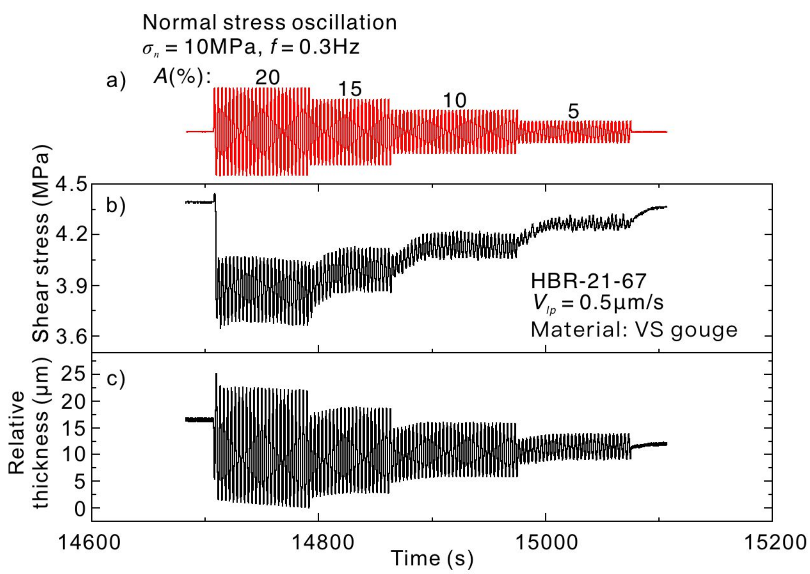

Figure 8. VS gouge. Result of NSO experiment conducted with different oscillation amplitude (5–20%) when using chlorite as simulated gouge. The oscillation frequency was kept constant at 0.6 Hz. The background normal stress is 10 MPa. a) Applied normal stress. b) Shear stress. (c) Fault thickness change. The fault displacement is not shown since the LVDT failed during this period.

4 Discussion of the experimental results

4.1 Comparison between SVW and VS Samples

Previous room-temperature NSO experiments performed using quartz (velocity-strengthening) shows similar results (Boettcher & Marone, 2004) to those obtained for the VS gouge in this study, though different experimental conditions were adopted. Like us, Boettcher & Marone (2004) also observed dynamic weakening during medium/high-frequency NSO and a sawtooth-shaped shear stress waveform during high-frequency NSO. Therefore, in this study, we assume that our experimental results for chlorite are representative for a VS gouge and can be compared with the SVW gouge despite the different experimental conditions. Both our SVW and VS gouges exhibit fault weakening at large oscillation frequency (Figs. 3 and 7) and amplitude (Figs. 4 and 8). Moreover, fault weakening increases with oscillation amplitude in both cases. The decrease in the average shear strength with increasing oscillation amplitude presumably reflects increased fault dilation, since fault weakening is always associated with fault dilation as indicated by our transmitted ultrasonic waves measurements (Fig. 5). The main difference in behavior between our SVW vs. VS materials under NSO conditions is that unstable events can be triggered by NSO only in the SVW material, notably at the medium oscillation frequencies (0.03–0.1 Hz, Fig. 3) and high amplitudes (15% and 20%, Fig. 4) investigated in this study.

4.2 Characteristic weakening frequency of the SVW material

To further investigate how the shear strength of the SVW material tested is modulated by different oscillation frequencies, we define two parameters: $\Delta\tau$ and $\Delta\tau_w$ (Fig. 9). $\Delta\tau$ represents shear stress fluctuations due to NSO. $\Delta\tau_w$ describes the extent of fault weakening, which is average shear strength after imposing NSO minus that before imposing NSO. The mechanical data for the SVW gouge shown in Fig. 3 was first separated into several segments where each segment corresponds to a single oscillation frequency (the sudden drop of shear stress at the onset of NSO is excluded). Then we picked $\Delta\tau$ and $\Delta\tau_w$ in these segments. Fig. 10a shows the results for $\Delta\tau$, in which data points were colored according to the maximum velocity of fault slip associated with each shear stress drop, as derived from LVDT displacement data. When the oscillation frequency is less than 0.05 Hz, $\Delta\tau$ is much larger than determined at other oscillation frequencies, due to the direct coupling between normal stress and shear stress via the friction coefficient. At oscillation frequencies ranging from 0.04 to 1 Hz, we can observe a baseline $\Delta\tau$ value around 0.2 MPa. However, when the oscillation frequency reaches around 0.1 Hz, $\Delta\tau$ values reach a maximum and then decrease with increasing oscillation frequency. Significant fault weakening $\Delta\tau_w$ also occurs at around 0.05 Hz (Fig. 10b), and can be regarded as a second-order effect of the amplified $\Delta\tau$. Therefore, in this study, we refer to the NSO frequency ranging from 0.05 to 0.1 Hz as the "characteristic frequency", meaning $\Delta\tau$ and $\Delta\tau_w$ significantly amplify when the oscillation frequency falls in this range. What is interesting is that the fault slip velocity associated with shear stress drop, as recorded by the LVDT attached to the central sliding block, also peaks at 0.1 Hz, suggesting that the fault reaches an unstable state at the characteristic frequency. The recorded fault velocity is up to 100 μm/s. Given that the broadband acoustic sensor used to receive the transmitted ultrasonic waves can also receive the signal from other passive sources (e.g., laboratory earthquakes), it is possible for us to investigate the slip modes (aseismic or seismic) of the unstable slip events observed in the SVW material. To do this, we examine the amplitude spectra of the received acoustic signal in a range of frequencies from 0 to 600 kHz. Bolton et al. (2022) reported that the dominant frequency of the acoustic emission signal for lab earthquakes is distributed between 100 kHz and 500 kHz. However, in the case of the instantaneous event at the onset of NSO (an event with the largest $\Delta\tau$ and largest slip rate observed in this study), we find that there is no signal detected in this frequency range alongside the stress drop (Fig. S7), suggesting that the slip is probably aseismic.

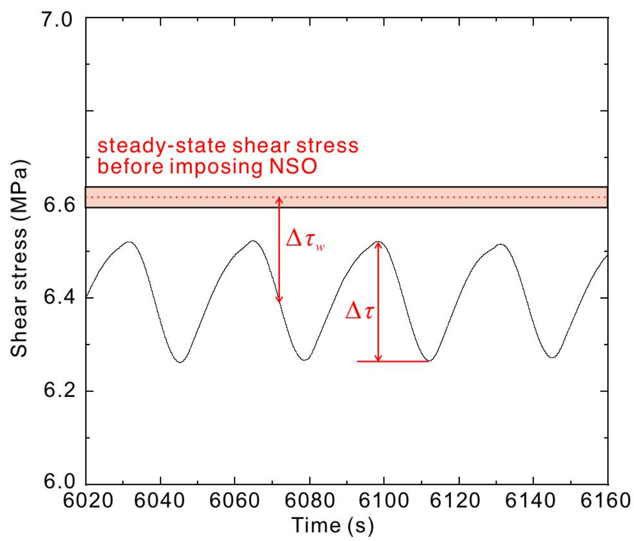

Figure 9 Definition of $\Delta\tau$ and $\Delta\tau_w$. Here $\Delta\tau$ refers to the amplitude of shear stress fluctuation due to NSO. $\Delta\tau_w$ represents the extent of fault weakening, defined as average shear strength after imposing NSO minus that before imposing NSO.

In previous studies, amplification of shear stress and fault weakening due to NSO has been identified as a resonance phenomenon whereby a steadily creeping fault can be destabilized within specific parameter ranges. However, the conditions needed to excite resonance are strict. Specifically, the stiffness ratio k/k_c and the ratio of the imposed and critical oscillation period $T_{NSO}/T_{critical}$ must approach 1.0 (Rice & Ruina, 1983). At the same time, the oscillation amplitude must exceed a critical value $\boldsymbol{\varepsilon}_c$ (Perfettini et al., 2001). In some physics research, the oscillation rate, which is defined as the product of oscillation amplitude and frequency, is a primary factor that controls the occurrence of resonance (Vidal et al., 2019). In our experiment on SVW gouge, we observed resonant behavior under specific experimental settings (oscillation amplitude = 20%, oscillation frequency = 0.1 Hz, load-point velocity=0.25 m/s), giving rise to a maximum in

$\Delta\tau$ along with considerable fault weakening and high slip velocity (Fig. 10). However, the main factor for generating resonance in SVW gouge is not clear and thus requires more experimental research in the future.

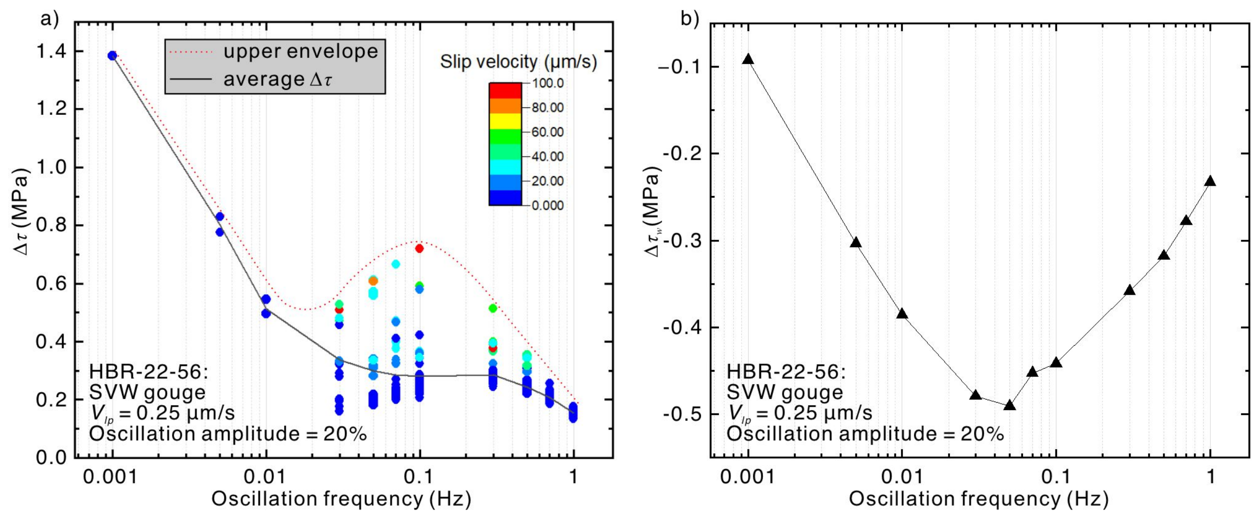

Figure 10 Effect of NSO frequency on $\Delta\tau$ (a) and $\Delta\tau_w$ (b). In Figure (a), each data point refers to the value of $\Delta\tau$ for each oscillation cycle. The color represents the maximum slip velocity accompanying each drop in shear stress, as derived from the LVDT displacement data. The solid black line shows the average $\Delta\tau$ for each oscillation frequency while the dashed red line shows the upper envelope of these data points.

5 Quantifying the Frictional Behavior of SVW Gouge Material during NSO using a Microphysical Model

We now attempt to explain our experimental results for SVW gouge, i.e. the effects of NSO on frictional slip and stability, by comparison with the microphysical model for the frictional properties of fault gouges proposed by Chen and Spiers (2016) – see also Niemeijer and Spiers (2007).

5.1 Model adaptation

The above authors proposed a microphysical model (referred to as the Chen-Niemeijer-Spiers or "CNS model"), which has successfully reproduced the quasi-state and transient frictional behavior of calcite gouge – based on a consideration of the deformation mechanisms operating at the grain scale. In this model, the geometric structure of the gouge layer is divided into two parts, namely a localized shear band and the remaining bulk gouge layer which does not participate in shearing by granular flow. Friction is mainly controlled by competition between grain scale creep processes and dilatant granular flow (intergranular sliding) within the shear band, with frictional interactions at grain contacts being inherently velocity-strengthening. The original assembly of the CNS model is as follows:

$$V_{imp} - \frac{\dot{\tau}}{K} = L_t\left[\lambda\dot{\gamma}_{ps}^{sb} + (1-\lambda)\dot{\gamma}_{ps}^{bulk}\right] + L_t\lambda\dot{\gamma}_{gr}^{sb} \tag{5a}$$

$$\frac{\dot{\varphi}^{sb}}{1-\varphi^{sb}} = (\tan\psi^{sb})\dot{\gamma}_{gr}^{sb} - \dot{\varepsilon}_{ps}^{sb} \tag{5b}$$

$$\tau = \frac{\tilde{\mu}+\tan\psi^{sb}}{1-\tilde{\mu}\tan\psi^{sb}}\sigma_n \tag{5c}$$

$$\tilde{\mu} = \tilde{\mu}^{*} + a_{\tilde{\mu}} \ln\left(\frac{\dot{\gamma}_{gr}^{sb}}{\dot{\gamma}_{gr}^{sb*}}\right) \tag{5d}$$

In these equations, Eq. (5a) describes the kinematics of the fault system in the shear direction, where V_{imp} is load-point velocity, τ is shear stress, L_t is the total thickness of the gouge layer, λ is the thickness ratio of the localized shear band, γ is shear strain. The superscripts "sb" and "bulk" represent shear band and bulk gouge layer quantities, while the subscripts "ps" and "gr" represent plastic flow (e.g. by pressure solution or any other creep mechanisms – Chen and Spiers (2016) mentioning other mechanisms) and granular flow, which are the two main deformation mechanisms that control macroscopic friction. Eq. (5b) applies to the shear band specifically and expresses compaction/dilation normal to the fault zone, whereby φ^{sb} and $\dot{\varepsilon}_{ps}^{sb}$ represent the porosity and compaction strain rate by plastic flow of grains within shear band. ψ is the mean dilation angle at grain contacts. φ^{sb} and ψ^{sb} can be seen as microstructural state variables in the shear band, which are related, following Niemeijer and Spiers (2007), by:

$$tan\psi^{sb} \approx H(q - 2\varphi^{sb}) \tag{6}$$

which also applies for $\varphi^{bulk}$and ψ^{bulk}. Here H is a geometric factor and $q = 2\varphi_c$is double the critical state porosity φ_c (the porosity for critical state granular flow familiar from soil mechanics) at which ψ reaches zero. Based on a regular pack that is filled with spherical grains, another porosity-dependent microstructural state variable, the mean grain-to-grain contact area a_c, can be approximated as:

$$a_c = \frac{\pi d^2(q-2\varphi)}{z} \tag{7}$$

where d is grain size, z is coordinate number (Niemeijer and Spiers, 2007).

The friction law in the CNS model is presented in Eq. (5c) where $\tilde{\mu}$ is grain boundary friction. This equation is derived from the energy/entropy balance for granular flow, which links shear stress and dilation angle. The grain boundary friction $\tilde{\mu}$ at the lattice scale can be expressed by Eq. (5d) where $a_{\tilde{\mu}}$ expresses its strain rate sensitivity and $\tilde{\mu}^*$ is the grain boundary friction at the reference of shear strain rate $\dot{\gamma}^*_{gr}$. Here $\dot{\gamma}^*_{gr}$ has the same function and physical significance as the reference velocity V^* in the RSF law, and can be thought of simply as a reference grain boundary shearing velocity v^* "normalized" with respect to the shear band thickness. From this equation, we can see that the grain boundary friction is intrinsically strain-rate strengthening. For more details about CNS model, readers can refer to recent literature (Chen & Niemeijer, 2017b; Chen et al., 2017; Chen & Spiers, 2016).

To apply the CNS model to conditions where normal stress oscillates during fault creep, some modifications are implemented in this study. The original model already incorporates effects of variable normal stress through the term $\dot{\varepsilon}^{sb}_{ps}$, which characterizes compaction strain rate resulting from compaction creep by plastic deformation of gouge grains, e.g., by pressure solution or dislocation creep. However, in the context of normal stress oscillation, 3 additional effects must be taken into account from a microphysical perspective:

1) **Elastic coupling between normal stress and shear stress**.

As shown in Fig. 11a, after applying normal stress oscillation, the load-point displacement shows a sinusoidal oscillation superimposed on a gradually increasing background value. This is a direct evidence for the elastic response of the sample assembly. From Eq. (5a), we know that the fault slip velocity V is the sum of shear creep rate and shear granular flow rate in the CNS model:

$$V = L_t\dot{\gamma} = L_t\left[\lambda\dot{\gamma}_{ps}^{sb} + (1-\lambda)\dot{\gamma}_{ps}^{bulk}\right] + L_t\lambda\dot{\gamma}_{gr}^{sb} \tag{8}$$

The enlarged figure in Fig. 11a reveals that increasing normal stress can result in a decrease of the displacement at load point, which is resulted from the elastic response of the sample assembly (sample plus surrounding forcing blocks) or the gouge anisotropy. In other words, increasing normal stress can result in a negative change of the fault shear strain in a DDS configuration. Therefore, we can introduce a negative term to describe such negative change $\Delta\gamma_{el}$:

$$\Delta\gamma_{el} = \frac{\Delta L}{L_t} = -\frac{\Delta\sigma_n}{G_\varphi} \tag{9}$$

Here, ΔL is the length change of the sample assembly due to elastic response, which is equal to the change of the load-point displacement. $\Delta\sigma_n$ is the change of the applied normal stress. G_φ is a calibratable modulus. Rewriting Eq. (9) as:

$$\Delta L = -\frac{L_t}{G_\varphi}\Delta\sigma_n \tag{10}$$

Here $\frac{L_t}{G_\varphi}$ can be seen as the reciprocal of a calibratable stiffness, which is related to the elastic response of the sample when imposing normal stress oscillation. Therefore, we can determine $\frac{L_t}{G_\varphi}$ through the linear fit between ΔL (i.e., relative change of the load-point displacement) and $\Delta\sigma_n$. In our experiments, the slope for the linear fitting curve is "-3.16e-12 m/Pa" (see Fig. 11b). This is an estimated value because Fig. 11b does not display a fully elastic behavior. L_t=3e-4 m (same as the value shown in Table2), we can obtain G_φ=9.5e7 Pa.

To introduce such elastic response into the CNS model, we can substitute Eq. (10) into Eq. (8), which yields:

$$V = L_t\dot{\gamma} = L_t\left[\lambda\dot{\gamma}_{ps}^{sb} + (1-\lambda)\dot{\gamma}_{ps}^{bulk}\right] + L_t\lambda\dot{\gamma_{gr}^{sb}} - \frac{L_t}{G_\varphi}\dot{\sigma_n} \tag{11}$$

Here $\dot{\sigma_n}$ represents the normal stressing rate. Replacing the right-hand side of. Eq.(5a) with Eq. (11) writes the whole assembly of the kinematic equation for the extended CNS model:

$$V_{imp} - \frac{\dot{\tau}}{K} = L_t\left[\lambda\dot{\gamma}_{ps}^{sb} + (1-\lambda)\dot{\gamma}_{ps}^{bulk}\right] + L_t\lambda\dot{\gamma_{gr}^{sb}} - \frac{L_t}{G_\varphi}\dot{\sigma_n} \tag{12}$$

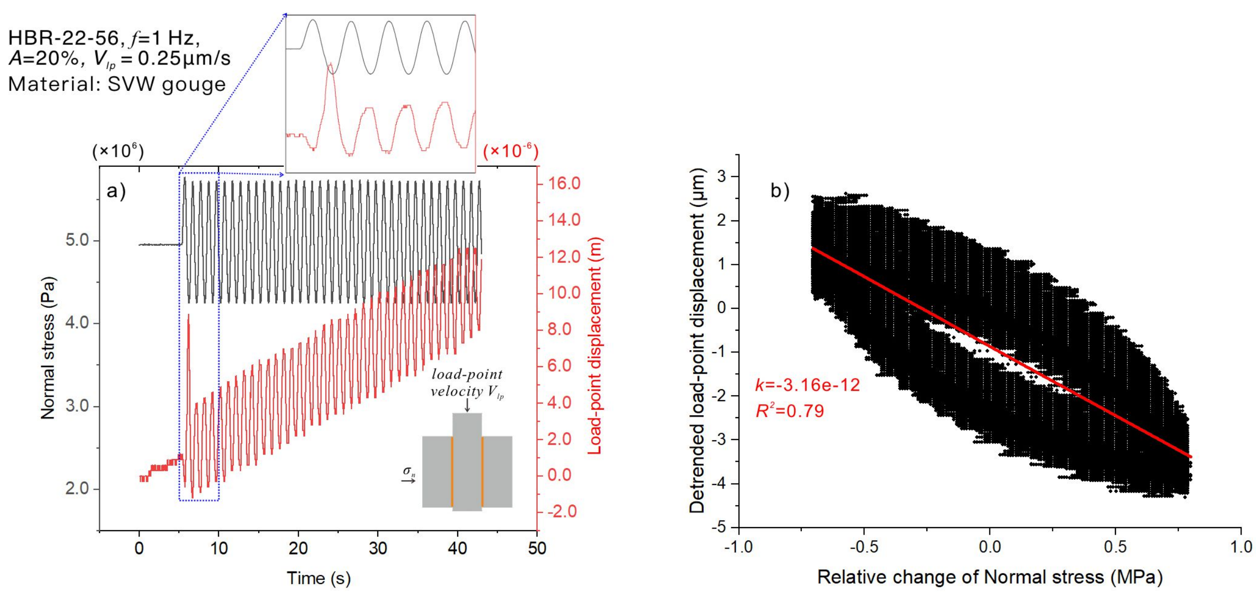

Figure 11 a) Evolution of the load-point displacement after imposing normal stress oscillation (*A*=20%, *f*=1 Hz); b) Relationship between the relative change of the applied normal stress and the detrended load-point displacement. The slope ($-\frac{L_t}{G_\varphi}$) for fitting curve

can be used to estimate the calibratable stiffness due to the elastic response and then calculate G_φ through a given L_t. However, it is an estimated value because the data does not show fully elastic behavior.

2) **Effects of gouge elasticity on porosity and grain contact area**. During the NSO period, gouge grains, no matter in shear band or bulk gouge layer, will undergo elastic deformation and hence cause changes in the volume of pore space. Therefore, the variation of porosity $\Delta\varphi$ due to this effect should be incorporated in the state evolution function of Eq. (5b), which applies for both shear band and bulk. Given that porosity must decrease elastically with increasing normal stress, we can write $\Delta\varphi = -\frac{\Delta\sigma_n}{E_\varphi}$, which in differential form yields $\Delta\dot{\varphi} = -\frac{\dot{\sigma_n}}{E_\varphi}$ where E_φ is the mean effective compression modulus of the gouge layer. In addition, when the fault gouge is subjected to a rapid increase in normal stress, the grain contact area will increase immediately (in shear band and bulk) due to elastic distortion. Here we account for this effect by assuming it can be treated independently of changes in porosity, i.e., by modifying Eq. (7) to the form:

$$a_c = \frac{\pi d^2\left(q - 2\varphi + \beta\frac{\Delta\sigma_n}{\sigma_n^0}\right)}{z} \tag{13}$$

where β is a dimensionless elastic proportionality factor and σ_n^0 is the reference normal stress. Elastic changes in the dilation angle due to NSO can also be expected, as well as in porosity and grain contact area, of course. As a first approximation, we assume these to be determined by the difference between q and φ in Eq. (6).

3) **Effects of gouge elasticity on critical porosity.** Oscillating normal stress not only changes the porosity but also its critical value φ_c. We can introduce a variable $\Delta\varphi_c$ to

approximate this effect in the same way as for the gouge porosity, so we have $\Delta\dot{\varphi}_c = -\frac{\dot{\sigma}_n}{E_c}$ where E_c is the effective compression modulus of the gouge layer at critical state.

Adding terms representing the above effects into the original CNS equations (Eqs. (5a)–(5d)) now leads to the result:

$$V_{imp} - \frac{\dot{\tau}}{K} = L_t\left[\lambda\dot{\gamma}_{ps}^{sb} + (1-\lambda)\dot{\gamma}_{ps}^{bulk}\right] + L_t\lambda\dot{\gamma}_{gr}^{sb} - \frac{L_t}{G_\varphi}\dot{\sigma}_n \tag{14a}$$

$$\frac{\dot{\varphi}^{sb}}{1-\varphi^{sb}} = (tan\psi^{sb})\dot{\gamma}_{gr}^{sb} - \dot{\varepsilon}_{ps}^{sb} - \frac{\dot{\sigma}_n}{E_\varphi} \tag{14b}$$

$$\tau = \frac{\tilde{\mu} + tan\psi^{sb}}{1 - \tilde{\mu}tan\psi^{sb}}\sigma_n \tag{14c}$$

$$\tilde{\mu} = \tilde{\mu}^* + a_{\tilde{\mu}}\ln\left(\frac{\dot{\gamma}_{gr}^{sb}}{\dot{\gamma}_{gr}^{sb*}}\right) \tag{14d}$$

$$\frac{\dot{\varphi}_c}{1-\varphi_c} = -\frac{\dot{\sigma}_n}{E_c} \tag{14e}$$

5.2 Model implementation – simulation of SVW gouge behavior

In the following, we use the above model to simulate the NSO experiment on SVW gouge reported in Fig. 6, which includes a spontaneous event or instability induced during NSO. As seen in Eq. (14a), the total shear strain rate includes the sum of two irreversible (inelastic) components: contact creep caused by plastic deformation of the grains (by pressure solution or any other creep mechanisms) $\dot{\gamma_{pl}}$ and granular flow $\dot{\gamma_{gr}}$. According to Chen et al. (2017), different mechanisms dominate the fault friction sliding in low-, intermediate-, and high-velocity regimes. For example, in the low-velocity regime, plastic flow is the dominant mechanism, giving $\dot{\gamma_{pl}}/\dot{\gamma_{gr}} > 1$, so the resulting fault velocity refers to "low velocity". The dominant mechanism becomes granular flow in the intermediate-velocity regime ($\dot{\gamma_{pl}}/\dot{\gamma_{gr}} < 1$) then plastic flow dominates again in the high-velocity regime ($\dot{\gamma_{pl}}/\dot{\gamma_{gr}} \gg 1$) due to some thermally activated mechanisms, such as flash heating. In this study, we assume the experimental condition (V_{imp}=1e-8–0.1 m/s) shown in Fig. 6 falls in the in the intermediate-velocity regime (Chen et al., 2017), where shear deformation is expected to be mainly controlled by granular flow in the shear band. Therefore, the shear creep strain rates caused by plastic deformation of the SVW gouge, $\dot{\gamma}_{ps}^{sb}$ and $\dot{\gamma}_{ps}^{bulk}$, can be ignored and set to zero. However, plastic deformation of the SVW gouge is assumed to contribute to compaction, since very low rates can have a significant impact in competition with minor dilation due to granular flow. To quantify the normal compaction strain rate due to contact creep within both shear band and bulk gouge layer, we use the following empirical function:

$$\dot{\varepsilon_{pl}} = B f_{pl}(\varphi) \tag{15}$$

Here B is a measure of the creep rate of dense gouge material, equal to $A_{pl} \frac{\sigma_n^p}{d^m} exp\left(-\frac{E_a}{RT}\right)$, as described by Hunfeld et al. (2019), where A_{pl} is a temperature-independent constant, p is stress exponent, d is the grain size, m is the grain sensitivity exponent, E_a is the activation energy, R is the gas constant, T is the temperature. Note that at constant applied stress, temperature and for a fixed material with given grain size, B is constant – or near-constant for small and/or rapid oscillations in applied normal stress. $f_d(\varphi)$ is the porosity function accounting for changes in contact area caused by compaction, which can be written as (Spiers et al., 2004):

$$f_{pl}(\varphi) = \left(1 - \frac{\varphi}{\varphi_c}\right)^{-M} \tag{16}$$

where M describes the sensitivity to changes in porosity. Substituting Eq. (16) into Eq. (15) yields:

$$\dot{\varepsilon_{pl}} = B\left(1 - \frac{\varphi}{\varphi_c^{gouge}}\right)^{-M} \tag{17}$$

By fitting this function to φ and $\dot{\varepsilon_{pl}}$ data retrieved from a uniaxial compaction creep test conducted on the SVW gouge at the same temperature and reference normal stress used in our SVW shear experiment (Fig. S8), B, φ_c and M can be obtained, without specifically identifying the creep mechanism responsible (e.g., dislocation creep versus pressure solution made possible by adsorbed atmospheric humidity). The thus-fitted parameter values for calculating the compaction creep rate, as well as other parameters utilized in simulating our NSO shear experiment using the modified CNS model, are summarized in Table 2. For the newly introduced elastic parameters, E_φ can be estimated from the normal load cycling step performed before each run, because the thickness of the gouge layer can be measured precisely by the eddy current sensor. G_φ should be on the order of 9e7, which is obtained from the fitting result between the normal stress and the load-point displacement (Fig. 11b). The effective shear modulus of porous granular material must be lower than that of fully dense solid, so following previous work on effects of porosity on elastic parameters (Yu et al., 2016), at critical state ($\psi = 0$), the gouge layer will be even more porous and compliant, so we assume $E_c = E_\varphi/8$ here. β was estimated based on the scale factor between applied normal stress and total contact area of slip surface according to Dieterich and Kilgore (1996). In simulating laboratory experiments, we normally choose boundary conditions of constant normal stress and stepped load-point velocity (Chen et al., 2016). Here we impose constant load-point velocity with normal stress oscillation of varying periods. According to previous, studies, the periods are expected to interact with the characteristic time scales inherent in the processes incorporated in the model., including the characteristic time (D_c/V), the critical recurrence period of instability (Eq. (2)), and the time scale for plastic flow ($1/\dot{\varepsilon_{pl}}$). The estimated values for these time scales in our tests are given in Table S1.

Table 2 List of Parameters Used in NSO Simulation

Parameter	Description	Value	Data Source and References
σ_n	Effective normal stress (Pa)	5e6	Applied in experiments
A_n	Oscillation amplitude of NSO (Pa)	±0.25 (5%)	
F_n	The oscillation frequency of NSO (Hz)	0.07	
T	Temperature (K)	293.15	
V_{imp}	Load point velocity (m/s)	0.25e-6	
K	Machine stiffness (Pa/m)	3e10	Calibrated machine value
L_t	Thickness of gouge layer (m)	3e-4	Estimated from microstructure
λ	Localization degree	0.08	
d^{sb}	Average Grain size of shear band (m)	0.63e-6	
d^{bulk}	Average Grain size of bulk gouge layer (m)	2e-5	
φ_0^{bulk}	Initial porosity of bulk gouge layer	0.3	Experimentally observed value
z	Grain coordinate number	6	Following (Spiers et al., 2004)
H	Geometric factor	0.9	Following (Niemeijer & Spiers, 2007)
$\tilde{\mu}^*$	Reference grain boundary friction coefficient for velocity of $1e^{-6}$ m/s	0.73	Assumed here
$a_{\tilde{\mu}}$	The coefficient for logarithmic rate dependence of grain boundary friction	0.002	
β	Dimensionless proportionality factor to describe the effect of normal stress on the average contact area	0.3	Estimate from the data reported by Dieterich and Kilgore (1996)
B	Parameter used to describe the combined effects of normal stress, grain size and temperature on the fault compaction	1.17e-11	Derived by fitting the results of compaction test for the SVW gouge (Fig. S8) based on Eq. (17)
φ_c	Mean critical porosity	0.45	
M	Stress sensitivity to changes in porosity	7.72	
E_φ	Effective compression modules of the shear band (Pa)	2.4e8	Same order of magnitude as the modulus measured from normal load cycling (Fig. S3)
G_φ	Effective shear modules of the shear band (Pa)	6e7	Same order of magnitude as the calibratable modulus estimation (Fig. 11b)

E_c	Effective compression modules of the shear band at critical state (Pa)	3e7	Yu et al., 2016

As shown in Fig. 12b, the modeled shear stress in the simulation of the NSO experiment reported in Fig. 6 starts with a sinusoidal fluctuation followed by an unstable event (the first small stress drop event in Fig. 6b is not captured) and then recovers towards the starting value. The variation of shear stress and the stress drop associated with instability are of similar order of magnitude to those of the experimental results (Fig. 6). We also observe dilation of the gouge layer through the simulated and experimental thickness change (Fig. 12c), implying that the same evolution of microstructure accompanied the load drop in both cases. The difference in the order of magnitude of thickness can be attributed to inconsistent movement of two experimental faults in the DDS configuration, and/or a heterogeneous gouge thickness along the fault, for example.

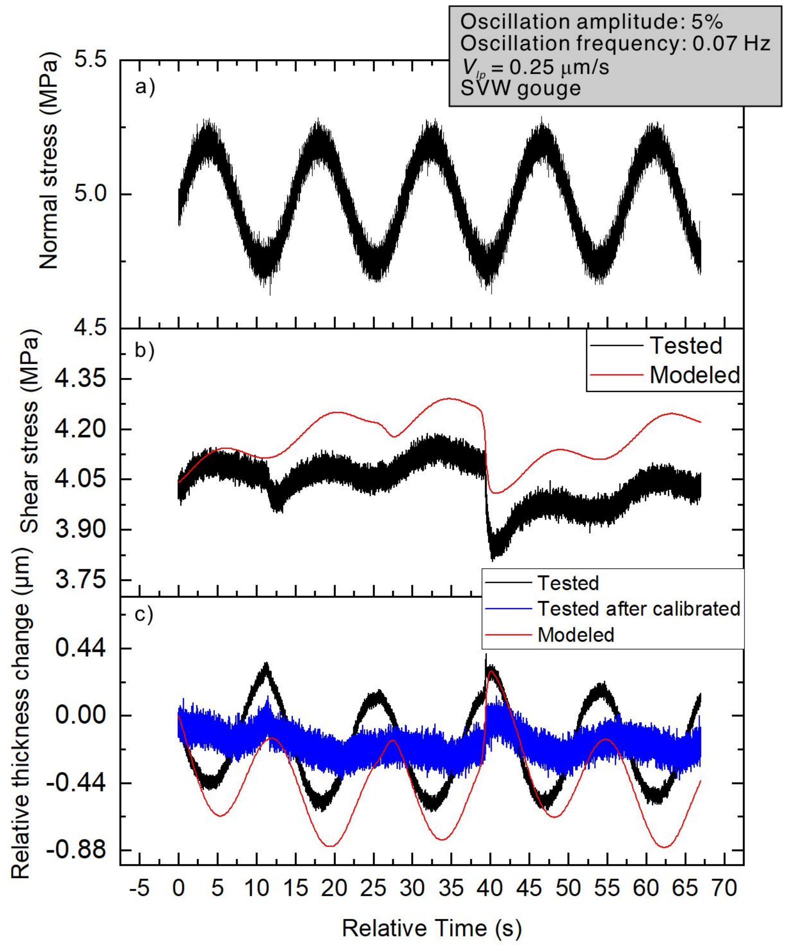

Figure 12 Comparison between experimental and modeled results based on the modified CNS model applied to the experiment reported in Fig 6. Applied normal stress (a) is the same as shown in Fig. 6a. (b) Modeled shear stress (red line) and that recorded in experiment (black line). (c) Modeled fault thickness (red line), the measured fault thickness (black line) and the data after calibrating the elastic component (blue).

6 Comparison between Modeled and Measured Transmitted Waves

Active ultrasonic waves can be used to probe the state of grain contacts within the sample during steady state fault shearing or during transient behavior (Chaize et al., 2023; Shreedharan et al., 2019; Yoshioka & Iwasa, 2006). From the microphysical perspective, one method to test the present modifications to the CNS model (Eqs. (14)) is to perform forward modeling of transmitted ultrasonic waves, considering the state of grain contact as captured by the model, and then compare the "predictions" with the test results. Based on classical theory of elastic wave propagation, we built a numerical model to simulate transmitted wave behavior under the same experimental conditions as depicted in Fig. 6b. In this model, the evolution of contact area (a_c) predicted by the modified CNS model is key (Eq. (13)). In this section, we will demonstrate the logic of how this model was built and compare the modeled results with those recorded in the experiment on SVW gouge represented in Fig. 6.

6.1 Sample Geometry and Background Knowledge

Based on the geometry of DDS as shown in Fig. 1b, we define W_o and W_i as the width of outer and inner granite blocks, respectively. L_t denotes the thickness of the gouge layer. A_0, represents the pressure amplitude of the incident wave, A_1, is the transmitted wave amplitude at the central point of the assembly, and A_f is that at the exit side (Fig. 13).

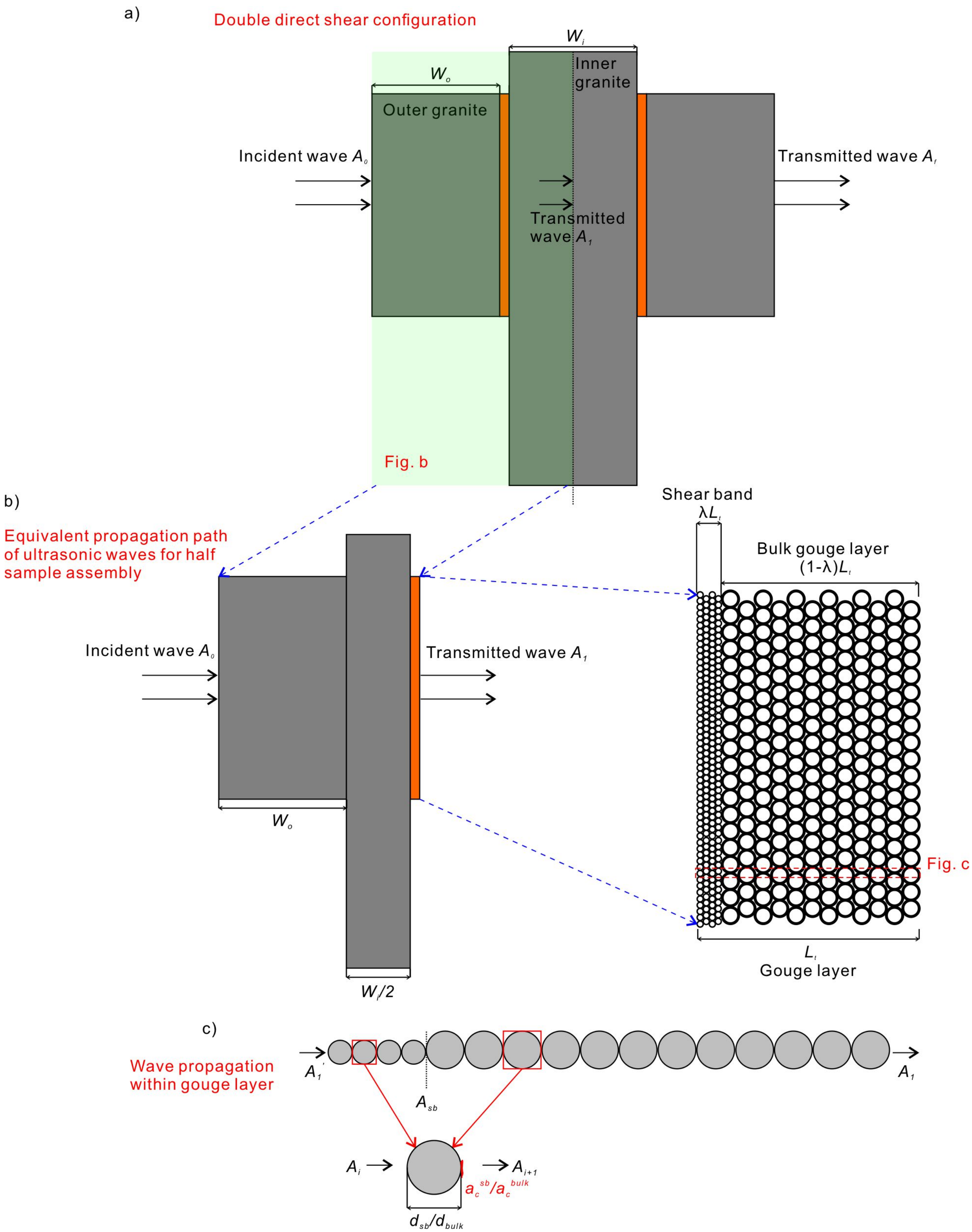

a)
Double direct shear configuration
W_i
W_o
Inner granite
Outer granite
Incident wave A_o
Transmitted wave A_t
Transmitted wave A_1
Fig. b
b)
Equivalent propagation path of ultrasonic waves for half sample assembly
Incident wave A_o
Transmitted wave A_1
W_o
$W_i/2$
Shear band
λL_t
Bulk gouge layer
$(1-\lambda)L_t$
Fig. c
L_t
Gouge layer
c)
Wave propagation within gouge layer
A_1'
A_{sb}
A_1
A_i
A_{i+1}
a_c^{sb}/a_c^{bulk}
d_{sb}/d_{bulk}

Figure 13. Schematic showing how elastic waves are assumed to propagate through the surrounding rock blocks and gouge layer in the present wave simulation. (a) Wave propagation through the whole DDS configuration. A_0, A_1, and A_f represent the amplitude of incident ultrasonic wave, the transmitted ultrasonic wave propagating to the center and the exit side of sample assembly. W_o and W_i represent the width of outer and inner granite, respectively. (b) Equivalent propagation path of the ultrasonic waves when considering that the waves propagate to the center of DDS sample assembly, including a granite with a thickness of $W_o+W_i/2$ and the fault gouge layer with a thickness of L_t. λ is the ratio of the shear band thickness to the whole gouge layer. (c) Propagation of ultrasonic waves within the fault gouge layer, in which the change of grain-to-grain contact area is considered. The amplitude of ultrasonic waves after traveling through the shear band is defined as A_{sb}.

According to the classical theory of elastic wave propagation, for the case of 1D transmission and attenuation in a continuum, the amplitude of the transmitted wave can be described as (Knopoff & MacDonald, 1958):

$$A = A_0 e^{-\xi x + i(kx - \omega t)} \tag{18}$$

where A_0 is the amplitude of incident wave, ξ is the attenuation factor, x is travel distance, k is wavenumber, ω is corner frequency, t is time. The reflection term is ignored in this study for simplicity, as it has minimal effects on the overall results.

6.2 Wave propagation in the DDS Assembly

Let us start with deducing the amplitude of transmitted P-waves at the central point of the DDS assembly (Fig. 13a), i.e. A_1. In this case, the travel path of elastic waves is equivalent to passage through the granite blocks with a width $W_o+W_i/2$ plus a single gouge layer, thickness L_t

(see the schematic in Fig. 13b). A_1' refers to the pressure amplitude of waves at the interface between the surrounding granite blocks and the gouge layer.

According to Eq. (18), A_1' in this new geometry can be written as:

$$A_1' = A_0 e^{-\xi_{gran}\left(W_0+\frac{W_i}{2}\right)+i\left[k\left(W_0+\frac{W_i}{2}\right)-\omega t\right]} \tag{19}$$

where ξ_{gran} is the attenuation factor of granite.

The gouge layer can be further divided into the shear band and bulk gouge zone in the framework of the CNS model, as observed in our experiments (Fig. S9). When we consider 1D propagation of elastic wave through the entire gouge layer (REV- representative elementary volume, shown in Fig. 13c), we can define A_{sb} as the amplitude at the exit surface of the shear band A_i and A_{i+1} represent the amplitude of elastic wave before and after transmitting through a single grain with a diameter d_{sb}, which can be written as:

$$A_{i+1} = A_i e^{-\xi_{gouge} d_{sb}+i[k d_{sb}-\omega t]} \cdot f(a_c) \tag{20}$$

where ξ_{gouge} is the attenuation factor of the gouge sample. We introduce a calibration function $f(a_c)$, aiming at accounting for the effects of grain contact area on transmitted amplitude of ultrasonic waves and linking contact area predicted by the modified CNS model to the progress of wave propagation. The main idea here is that elastic waves do not propagate in a continuum, but rather across the interfaces between grains, specifically at the contact area a_c which will continuously fluctuate during NSO. Nagata et al. (2014) conducted direct-shear experiments on the transparent Lucite and measured the contact area as well as stiffness at the same time using transmitted light and acoustic waves. They observed that the change in contact area was proportional to the change of transmission coefficient of acoustic waves during velocity-step and hold tests. However, two variables did not track each other when the simulated fault was subjected to a normal stress step. Kendall and Tabor (1997) demonstrated that the normal stiffness of multiple contacts depends on the size of contacts (i.e., the square root of contact area). In their model, when the contact number keeps constant, the normal stiffness of an interface filled with multiple contacts will not change despite the asperities grow with increasing normal stress because the envelope size of the contacts does not change. In this study, we attempt to simulate the response of transmission coefficient accompanied by an unstable event triggered by a low-frequency NSO (reported in Fig. 6), in which normal stress do not change abruptly. Moreover, we assume that the change of contact area keeps constant as it is hard to determine within the gouge layer. Therefore, we approximate $f(a_c)$ in equation (20) as the square root of contact area (as predicted by the modified CNS model) normalized by the grain size:

$$f(a_c) = \frac{\sqrt{a_c}}{d} \tag{21}$$

Here *d* represents the grain size of shear band d_{sb} or the bulk gouge layer d_{bulk}. We add this term because $f(a_c)$ has to be equal to 1 when the porosity reaches 0 so that propagation of elastic waves within a continuum can be achieved.

The amplitude at the exit surface of the shear band A_{sb} is the superposition of the waves propagated through each contact (Somfai et al., 2005), given:

$$A_{sb} = A_1'\left[e^{-\xi_{gouge}d_{sb}+i[kd_{sb}-\omega t]} \cdot f(a_c^{sb})\right] \cdot \frac{\lambda L_{real}}{d_{sb}} \tag{22}$$

where $L_{real}=nL_t$, which represents the real travel distance in the shear band due to random packing, and *n* is a magnification factor. a_c^{sb} is the area of contact between two grains within the shear band. The amplitude at the exit surface of gouge layer A_1 can be obtained in the same way:

$$A_1 = A_{sb} \cdot \left[e^{-\xi_{gouge}d_{bulk}+i[kd_{bulk}-\omega t]} \cdot f(a_c^{bulk})\right] \cdot \frac{(1-\lambda)L_{real}}{d_{bulk}} \tag{23}$$

where d_{bulk} is the grain diameter within bulk gouge layer. a_c^{bulk} is the area of contact between two grains within the bulk gouge layer. Substituting Eq. (19), and Eq. (22) into Eq. (23) then yields:

$$A_1 = A_0 \cdot \left\{ e^{-\xi_{gran}\left(W_0+\frac{W_i}{2}\right)+i\left[k\left(W_0+\frac{W_i}{2}\right)-\omega t\right]} \right\} \cdot \left[e^{-\xi_{gouge} d_{sb}+i[k d_{sb}-\omega t]} \cdot f(a_c^{sb}) \right] \cdot \ldots$$

$$\frac{\lambda L_{real}}{d_{sb}} \cdot \left[e^{-\xi_{gouge} d_{bulk}+i[k d_{bulk}-\omega t]} \cdot f(a_c^{bulk}) \right] \cdot \frac{(1-\lambda) L_{real}}{d_{bulk}} L \quad (24)$$

Now considering elastic wave propagation throughout the whole sample, the distance will be double that described in the above case. Considering the symmetric geometry of DDS, the amplitude of the transmitted wave at the end of travel path, denoted as A_f, can be expressed as follows:

$$A_f = A_0 \cdot \left\{ e^{-\xi_{gran}(2W_0+W_i)+i[k(2W_0+W_i)-\omega t]} \right\} \cdot \left[e^{-\xi_{gouge} d_{sb}+i[k d_{sb}-\omega t]} \cdot f(a_c^{sb}) \right] \cdot \ldots$$

$$\frac{2\lambda L_{real}}{d_{sb}} \cdot \left[e^{-\xi_{gouge} d_{bulk}+i[k d_{bulk}-\omega t]} \cdot f(a_c^{bulk}) \right] \cdot \frac{2(1-\lambda) L_{real}}{d_{bulk}} L \quad (25)$$

6.3 Modelling Results: Transmitted Ultrasonic Waves

We simulated the evolution of the normalized transmission coefficient based on Eq. (25), assuming identical experimental conditions to those depicted in Fig. 6. The parameters utilized here are summarized in Table S2.

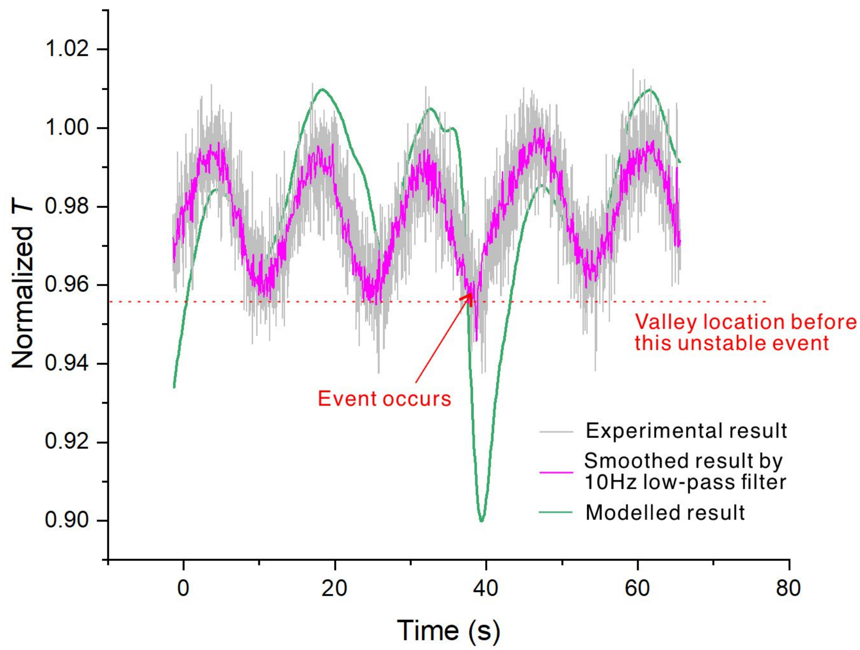

Figure 14 Contrast between modeled and recorded normalized transmission coefficient.

Fig. 14 displays the normalized value of the transmission coefficient of ultrasonic waves coming from experiment and simulation (for the original modelled waves, see Fig. S10). From the onset of NSO (an arbitrary zero time), both the experimentally determined and modeled *T* fluctuate sinusoidally with a similar frequency as normal and shear stress. An unstable event then occurs at $t \approx 30$ to 40 s, resulting in an instantaneous drop in the experimental and modeled transmission coefficient. The drop in simulated *T* is overestimated here, essentially due to an overestimate of the thickness change accompanied by this event (Fig. 12c). In addition, inaccuracy in estimating the attenuation of transmitted waves and the heterogeneity of DDS configuration might also explain this overestimate. However, both the predicted and experimental values of *T*, along with the correlation coefficient of the coda wave (Fig. 6e), effectively indicate fault dilation during an unstable slip event.

7 Implications for Induced Seismicity

Numerous field and associated modelling studies have shown that depletion of gas fields (Candela et al., 2019), gas storage reservoir cycling (Gao et al., 2022), repeated waste water injection (Goebel et al., 2017) and periodic hydraulic fracturing (Atkinson et al., 2016) cause variations in stress state on faults through the direct effect of pore pressure on effective stress and through the poroelastic response of the reservoir system (Segall & Lu, 2015). These changes in stress state have in turn been identified as the likely driver for induced seismicity. In this study, our results indicate that normal stress oscillation can not only lead to fault weakening but can also trigger unstable slip events when a fault is filled with SVW gouge materials, which are abundant in shallow sedimentary sequences and responsible for the transition from the stable to unstable regime (known as the upper stability transition of the seismogenic window within the continental crust, following Scholz (2018)) These unstable events are not stick-slip (i.e., laboratory earthquakes) but rather aseismic slip according to the amplitude spectrum analysis of the received ultrasonic signal (Fig. S7). Aseismic slip might pose some engineering risk, such as wellbore casing deformation (Zhang et al., 2022) and reservoir leakage (Feitz et al., 2022). If the Coulomb stress on fault is in a critical state, induced seismicity may occur despite minimal variation in stress (Lei et al., 2019). One possible reason is the effect of variable stress on the time-dependent nucleation process of earthquakes (Acosta et al., 2023; Dieterich, 1994). The other possible reason is the reduction of fault strength due to stress oscillation. As for VS gouge materials, unstable events are difficult to trigger but our experiments show that weakening still occurs under NSO with sufficiently large amplitude or at intermediate to high frequency (Figs. 7 and 8).

Injection volume (Hofmann et al., 2019; McGarr, 2014) and injection rate (Gori et al., 2021; Passelègue et al., 2018) are two main factors that influence induced slip behavior on fault zones. These two parameters determine the amplitude of stress variation along a fault in any given field situation. However, effects of oscillation frequency on fault stability need to be considered too, given that we found a characteristic frequency at which variation of shear stress and fault weakening can amplify. The value of this characteristic frequency is affected by many factors, such as load point velocity (Boettcher & Marone, 2004) and stiffness of surrounding material(Vidal et al., 2019), and requires further investigation in future.

The present study has shown that transmitted ultrasonic waves can be used to probe the grain contact state within shearing layers of simulated fault gouge. Among those parameters that are extracted from the transmitted waveforms, the coda wave correlation coefficient is the most closely correlated with changes of fault strength produced when imposing NSO (see Figs. 5e and 6e). In future, coda wave data may therefore offer potential for operators to monitor fault stability in a field case.

It is difficult if not impossible for experiments to replicate conditions consistent with field situations, especially regarding oscillation frequency and load-point velocity. For example, in the Groningen gas field of the Netherlands, variation of Coulomb stress change averaged over the whole gas field has been historically seasonal, with an amplitude up to ~9 kPa (see the detrending data presented by Acosta et al. (2023)). Therefore, a suitable friction model is necessary to extrapolate the experimental results to the field situation. We have extended the already existing CNS model to include effects of oscillating normal stress. The modified model can reproduce the mechanical data of experiments. Moreover, the microstructural evolution predicted by the model and recorded through the transmitted ultrasonic waves are in good agreement, which supports the current model. For further application in evaluating induced seismicity hazard, more variables should be investigated to test model robustness, and effects of factors such as load point velocity, machine stiffness, and the mode of stress perturbation. Of particular importance is to extend the range of NSO frequency and magnitude investigated in experiments to allow (or constrain model) extrapolation to field scenarios. Finally, besides proposing an acceptable model that can characterize fault friction, an accurate examination of stress field changes caused by pore pressure change is also necessary for the assessment of induced seismicity in reservoir systems undergoing periodic injection and/or depletion.

8 Conclusions

This study has investigated the influence of normal stress oscillation (NSO) on the frictional behavior and wave transmission properties of a fault zone prone to self-sustained oscillation under constant normal stress and load-point shear velocity, (i.e., a fault zone characterized by slightly velocity-weakening (SVW) behavior of the type often expected in shallow crustal faults). We measured the frictional strength of simulated SVW fault gouge layers, using a double-direct-shear and gouge-rock sample assembly. The experimental faults were subjected to a sinusoidally oscillating normal stress (frequency 0.001–1 Hz, amplitude 5%–20% of background normal stress). An active ultrasonic source was employed to probe the grain contact state within the gouge layers. Control experiments were also performed on a velocity strengthening or VS gouge (chlorite) to isolate aspects of mechanical behavior specific to slightly velocity-weakening fault rock. As for the SVW gouge, normal stress oscillation not only resulted in fault weakening but also triggered unstable slip events, especially at high amplitude and high frequency. We also found a characteristic frequency at which variation of shear stress is significantly amplified and maximum fault weakening is achieved. Increasing the oscillation amplitude increased the extent of weakening and triggered more unstable events, which we suggest were aseismic, on the basis of amplitude spectrum analysis of the received acoustic signal. The measured fault displacement rate accompanying these unstable events is up to 100 μm/s. Three parameters were extracted from the transmitted ultrasonic waves, including the transmission coefficient, the wave velocity, and coda wave correlation coefficient. The results show that both fault weakening and triggered events are associated with fault dilation caused by normal stress oscillation. Our experiments on velocity-strengthening gouge (chlorite) showed that fault weakening also occurs at intermediate to high oscillation frequencies. However, no unstable slip events were observed, probably due to the inherent slip stability (velocity strengthening nature) of chlorite gouge.

The CNS (Chen-Niemeijer-Spiers) model is based on the microphysical processes operating during fault sliding We extended this model to include effects of elastic response of the sample assembly and the gouge microstructure during normal stress oscillation, with the aim of reproducing the effects of NSO on fault shear strength and stability. Model results and the mechanical test data are in good agreement. To further validate the microstructural evolution captured by the modified model, we implemented forward modeling of transmitted ultrasonic waves, incorporating the evolution of grain-to-grain contact area a_c as predicted by the model. Both the modeled transmission coefficient and predicted mechanical behavior reflect the dilatancy observed to accompany the propagation of an instability. Application of the model to explore the effects of NSO on natural fault stability requires testing model performance using a wider range of input variables and parameters such as load-point velocity, stiffness of the surrounding medium, oscillation frequency and amplitude.

Acknowledgments

This study was supported by the National Natural Science Foundation of China (grants U1839211 and U2239204 to Shengli Ma, grant 42174224 to Jianye Chen). The work was also supported in part by the DeepNL research programme (Science4Steer Project, project number DEEP.NL.2018.046), financed by the Dutch Research Council (NWO). B.Yu acknowledges the China Scholarship Council for providing funding to perform the theoretical part of this study at Utrecht University. We thank Yanshuang Guo, Jiahui Feng and Qingbao Duan for the technique help in running the friction experiments and the compaction test. We thank the editor Prof. Alexandre Schubnel, an anonymous associated editor, an anonymous reviewer, and Prof. John W. Rudnicki for the constructive suggestions on this work.

Open Research

Original data corresponding to the main results shown in Fig. 3 to Fig. 8 is available at Yu et al. (2024).

References

Acosta, M., Avouac, J.-P., Smith, J. D., Sirorattanakul, K., Kaveh, H., & Bourne, S. J. (2023). Earthquake Nucleation Characteristics Revealed by Seismicity Response to Seasonal Stress Variations Induced by Gas Production at Groningen. *Geophysical Research Letters*, *50*(19), e2023GL105455. https://doi.org/10.1029/2023GL105455

Amemoutou, A., Martínez-Garzón, P., Kwiatek, G., Rubinstein, J., & Bohnhoff, M. (2021). Earthquake Source Mechanisms and Stress Field Variations Associated with Wastewater Induced Seismicity in Southern Kansas, USA. *Journal of Geophysical Research: Solid Earth*, *n/a*(n/a), e2020JB021625. https://doi.org/10.1029/2020JB021625

Atkinson, G. M., Eaton, D. W., Ghofrani, H., Walker, D., Cheadle, B., Schultz, R., Shcherbakov, R., Tiampo, K., Gu, J., Harrington, R. M., Liu, Y., van der Baan, M., & Kao, H. (2016). Hydraulic Fracturing and Seismicity in the Western Canada Sedimentary Basin. *Seismological Research Letters*, *87*(3), 631–647. https://doi.org/10.1785/0220150263

Baumberger, T., Berthoud, P., & Caroli, C. (1999). Physical analysis of the state- and rate-dependent friction law. II. Dynamic friction. *Physical Review B*, *60*(6), 3928–3939. https://doi.org/10.1103/PhysRevB.60.3928

Beeler, N. M., Tullis, T. E., Blanpied, M. L., & Weeks, J. D. (1996). Frictional behavior of large displacement experimental faults. Journal of Geophysical Research: Solid Earth, 101(B4), 8697–8715. https://doi.org/10.1029/96JB00411

Beeler, N., & Lockner, D. (2003). Why earthquakes correlate weakly with the solid Earth tides: Effects of periodic stress on the rate and probability of earthquake occurrence. *Journal of Geophysical Research*, *108*, 2391. https://doi.org/10.1029/2001JB001518

Beeler, N., Nagata, K., Kilgore, B., & Nakatani, M. (2010). Simultaneous measurement of real contact area and fault normal stiffness during frictional sliding. *AGU Fall Meeting Abstracts*.

Boatwright, J., & Cocco, M. (1996). Frictional constraints on crustal faulting. *Journal of Geophysical Research: Solid Earth*, *101*(B6), 13895–13909. https://doi.org/10.1029/96JB00405

Boettcher, M. S., & Marone, C. (2004). Effects of normal stress variation on the strength and stability of creeping faults. *Journal of Geophysical Research: Solid Earth*, *109*(B3), B03406. https://doi.org/10.1029/2003JB002824

Bolton, D. C., Shreedharan, S., McLaskey, G. C., Rivière, J., Shokouhi, P., Trugman, D. T., & Marone, C. (2022). The High-Frequency Signature of Slow and Fast Laboratory Earthquakes. *Journal of Geophysical Research: Solid Earth*, *127*(6), e2022JB024170. https://doi.org/10.1029/2022JB024170

Bureau, L., Baumberger, T., & Caroli, C. (2000). Shear response of a frictional interface to a normal load modulation. *Physical review. E, Statistical physics, plasmas, fluids, and related interdisciplinary topics*, *62, 6810–6820*. https://doi.org/10.1103/PhysRevE.62.6810

Cacace, M., Hofmann, H., & Shapiro, S. A. (2021). Projecting seismicity induced by complex alterations of underground stresses with applications to geothermal systems. *Scientific Reports*, *11*(1), 23560. https://doi.org/10.1038/s41598-021-02857-0

Candela, T., Osinga, S., Ampuero, J.-P., Wassing, B., Pluymaekers, M., Fokker, P. A., van Wees, J.-D., de Waal, H. A., & Muntendam-Bos, A. G. (2019). Depletion-Induced Seismicity at the Groningen Gas Field: Coulomb Rate-and-State Models Including Differential Compaction Effect. *Journal of Geophysical Research: Solid Earth*, *124*(7), 7081–7104. https://doi.org/10.1029/2018JB016670

Cao, W., Verdon, J. P., & Tao, M. (2022). Coupled Poroelastic Modeling of Hydraulic Fracturing-Induced Seismicity: Implications for Understanding the Post Shut-In ML 2.9 Earthquake at the Preston New Road, UK. *Journal of Geophysical Research: Solid Earth*, *127*(3), e2021JB023376. https://doi.org/10.1029/2021JB023376

Carpenter, B. M., Collettini, C., Viti, C., & Cavallo, A. (2016). The influence of normal stress and sliding velocity on the frictional behaviour of calcite at room temperature: insights from laboratory experiments and microstructural observations. *Geophysical Journal International*, *205*(1), 548–561. https://doi.org/10.1093/gji/ggw038

Chaize, E., Vieville, E., Valiorgue, F., & Courbon, C. (2023). An ultrasonic array-based method for the in-situ monitoring of contact area and wear under severe sliding conditions. *Wear*, 523, 204794. https://doi.org/10.1016/j.wear.2023.204794

Chambon, G., and J. W. Rudnicki (2001), Effects of normal stress variations on frictional stability of a fluid-infiltrated fault, *Journal of Geophysical Research: Solid Earth*, 106(B6), 11353–11372, https://doi.org/10.1029/2001JB900002.

Chanard, K., Nicolas, A., Hatano, T., Petrelis, F., Latour, S., Vinciguerra, S., & Schubnel, A. (2019). Sensitivity of Acoustic Emission Triggering to Small Pore Pressure Cycling Perturbations During Brittle Creep. Geophysical Research Letters, 46(13), 7414–7423. https://doi.org/10.1029/2019GL082093

Chen, J., Niemeijer, A., & Spiers, C. (2017). Microphysically Derived Expressions for Rate-and-State Friction Parameters, a , b , and D c: Microphysically Derived RSF Parameters. *Journal of Geophysical Research: Solid Earth*, 122(12), 9627–9657. https://doi.org/10.1002/2017JB014226

Chen, J., & Niemeijer, A. (2017). Seismogenic Potential of a Gouge-filled Fault and the Criterion for Its Slip Stability: Constraints From a Microphysical Model: Fault Stability Criterion. *Journ* *al of Geophysical Research: Solid Earth*, 122(12), 9658–9688. https://doi.org/10.1002/2017JB014228

Chen, J., & Spiers, C. (2016). Rate and state frictional and healing behavior of carbonate fault gouge explained using microphysical model: Microphysical model for friction. *Journal of Geophysical Research: Solid Earth*, 121(12), 8642–8665. https://doi.org/10.1002/2016JB013470

Chen, Z., Shi, L., & Xiang, D. (2017). Mechanism of casing deformation in the Changning–Weiyuan national shale gas demonstration area and countermeasures. *Natural Gas Industry B*, *4*(1), 1–6. https://doi.org/10.1016/j.ngib.2017.07.001

Cochard, A., Bureau, L., & Baumberger, T. (2003). Stabilization of Frictional Sliding by Normal Load Modulation. *Journal of Applied Mechanics*, *70*(2), 220–226. https://doi.org/10.1115/1.1546241

Colledge, M., Aubry, J., Chanard, K., Pétrélis, F., Duverger, C., Bollinger, L., & Schubnel, A. (2023). Susceptibility of Microseismic Triggering to Small Sinusoidal Stress Perturbations at the Laboratory Scale. Journal of Geophysical Research: Solid Earth, 128(4), e2022JB025583. https://doi.org/10.1029/2022JB025583

Dieterich, J. (1994). A constitutive law for rate of earthquake production and its application to earthquake clustering. *Journal of Geophysical Research: Solid Earth*, *99*(B2), 2601–2618. https://doi.org/10.1029/93JB02581

Dieterich, J. H. (1979). Modeling of rock friction: 1. Experimental results and constitutive equations. *Journal of Geophysical Research: Solid Earth*, *84*(B5), 2161–2168. https://doi.org/10.1029/JB084iB05p02161

Dieterich, J. H., & Kilgore, B. D. (1996). Imaging surface contacts: power law contact distributions and contact stresses in quartz, calcite, glass and acrylic plastic. *Tectonophysics*, *256*(1), 219–239. https://doi.org/10.1016/0040-1951(95)00165-4

Dieterich, J. H., & Linker, M. F. (1992). Fault stability under conditions of variable normal stress. *Geophysical Research Letters*, *19*(16), 1691–1694. https://doi.org/10.1029/92GL01821

Ellsworth, W. L., Giardini, D., Townend, J., Ge, S., & Shimamoto, T. (2019). Triggering of the Pohang, Korea, Earthquake (Mw 5.5) by Enhanced Geothermal System Stimulation. *Seismological Research Letters*, *90*(5), 1844–1858. https://doi.org/10.1785/0220190102

Farquharson, J., Heap, M. J., Baud, P., Reuschlé, T., & Varley, N. R. (2016). Pore pressure embr ittlement in a volcanic edifice. Bulletin of Volcanology, 78(1), 6. https://doi.org/10.1007/s00445-015-0997-9

Feitz, A., Radke, B., Ricard, L., Glubokovskikh, S., Kalinowski, A., Wang, L., Tenthorey, E., Schaa, R., Tertyshnikov, K., Schacht, U., Chan, K., Jordana, S., Vialle, S., Harris, B., Lebedev, M., Pevzner, R., Sidenko, E., Ziramov, S., Urosevic, M., Green, S., Ennis-King, J., Coene, E., Laviña, M., Abarca, E., Idiart, A., Silva, O., Grandia, F., Sainz-García, A., Takemura, T., Dewhurst, D., & Credoz, A. (2022). The CO2CRC Otway shallow CO2 controlled release experiment: Fault characterization and geophysical monitoring design. *International Journal of Greenhouse Gas Control*, *118*, 103667. https://doi.org/10.1016/j.ijggc.2022.103667

Gao, G., Chang, C., Wang, C., Li, Y., & Jia, J. (2022). Stress State Change and Fault-Slip Tendency Assessment Associated with Gas Injection and Extraction in the Hutubi (China) Underground Gas Storage. *SPE Journal*, 28(01), 446–461. https://doi.org/10.2118/212279-PA

Gheibi, A., & Hedayat, A. (2020). Ultrasonic imaging of microscale processes in quartz gouge during compression and shearing. *Journal of Rock Mechanics and Geotechnical Engineering*, *12*(06), 1137–1151. https://doi.org/10.1016/j.jrmge.2020.03.011

Glubokovskikh, S., Saygin, E., Shapiro, S., Gurevich, B., Isaenkov, R., Lumley, D., Nakata, R., Drew, J., & Pevzner, R. (2022). A small CO2 leakage may induce seismicity on a sub-seismic fault in a good-porosity clastic saline aquifer. Geophysical Research Letters, 49(12), e2022GL098062. https://doi.org/10.1029/2022GL098062

Goebel, T., Weingarten, M., Chen, X., Haffener, J., & Brodsky, E. (2017). The 2016 Mw5.1 Fairview, Oklahoma earthquakes: Evidence for long-range poroelastic triggering at >40 km from fluid disposal wells. *Earth and Planetary Science Letters*, *472*, 50–61. https://doi.org/10.1016/j.epsl.2017.05.011

Gori, M., Rubino, V., Rosakis, A. J., & Lapusta, N. (2021). Dynamic rupture initiation and propagation in a fluid-injection laboratory setup with diagnostics across multiple temporal scales. *Proceedings of the National Academy of Sciences*, *118*(51), e2023433118. https://doi.org/10.1073/pnas.2023433118

Gupta, H. K. (2002). A review of recent studies of triggered earthquakes by artificial water reservoirs with special emphasis on earthquakes in Koyna, India. *Earth-Science Reviews*, *58*(3), 279–310. https://doi.org/10.1016/S0012-8252(02)00063-6

Hadizadeh, J., Tullis, T. E., White, J. C., & Konkachbaev, A. I. (2015). Shear localization, velocity weakening behavior, and development of cataclastic foliation in experimental granite gouge. Journal of Structural Geology, 71, 86–99. https://doi.org/10.1016/j.jsg.2014.10.013

Harris, R. A. (1998). Introduction to Special Section: Stress Triggers, Stress Shadows, and Implications for Seismic Hazard. *Journal of Geophysical Research: Solid Earth*, *103*(B10), 24347–24358. https://doi.org/10.1029/98JB01576

Gutenberg, B., & Richter, C. F. (1944). Frequency of earthquakes in California*. Bulletin of the Seismological Society of America, 34(4), 185–188. https://doi.org/10.1785/BSSA0340040185

Heaton, T. H. (1975). Tidal Triggering of Earthquakes*. *Geophysical Journal International*, *43*(2), 307–326. https://doi.org/10.1111/j.1365-246X.1975.tb00637.x

Hill, D. P., Reasenberg, P. A., Michael, A., Arabaz, W. J., Beroza, G., Brumbaugh, D., Brune, J. N., Castro, R., Davis, S., Depolo, D., Ellsworth, W. L., Gomberg, J., Harmsen, S., House, L., Jackson, S. M., Johnston, M. J., Jones, L., Keller, R., Malone, S., Munguia, L., Nava, S., Pechmann, J. C., Sanford, A., Simpson, R. W., Smith, R. B., Stark, M., Stickney, M., Vidal, A., Walter, S., Wong, V., & Zollweg, J. (1993). Seismicity remotely triggered by the magnitude 7.3 landers, california, earthquake. *Science (New York, N.Y.)*, *260*(5114), 1617–1623. https://doi.org/10.1126/science.260.5114.1617

Hofmann, H., Zimmermann, G., Farkas, M., Huenges, E., Zang, A., Leonhardt, M., Kwiatek, G., Martinez-Garzon, P., Bohnhoff, M., Min, K.-B., Fokker, P., Westaway, R., Bethmann, F., Meier, P., Yoon, K. S., Choi, J. W., Lee, T. J., & Kim, K. Y. (2019). First field application of cyclic soft stimulation at the Pohang Enhanced Geothermal System site in Korea. *Geophysical Journal International*, *217*(2), 926–949. https://doi.org/10.1093/gji/ggz058

Hong, T., & Marone, C. (2005). Effects of normal stress perturbations on the frictional properties of simulated faults. *Geochemistry, Geophysics, Geosystems*, *6*(3), Q03012. https://doi.org/10.1029/2004GC000821

Hunfeld, L. B., Chen, J., Niemeijer, A. R., & Spiers, C. J. (2019). Temperature and Gas/Brine Content Affect Seismogenic Potential of Simulated Fault Gouges Derived From Groningen Gas Field Caprock. *Geochemistry, Geophysics, Geosystems*, *20*(6), 2827–2847. https://doi.org/10.1029/2019GC008221

Kaproth, B. M., and C. Marone (2014), Evolution of elastic wave speed during shear-induced damage and healing within laboratory fault zones, *Journal of Geophysical Research: Solid Earth*, 119, 4821–4840, doi:https://doi.org/10.1002/2014JB011051.

Kendall, K., & Tabor, D. (1997). An utrasonic study of the area of contact between stationary and sliding surfaces. *Proceedings of the Royal Society of London. A. Mathematical and Physical Sciences*, *323*(1554), 321–340. https://doi.org/10.1098/rspa.1971.0108

Keranen, K. M., Savage, H. M., Abers, G. A., & Cochran, E. S. (2013). Potentially induced earthquakes in Oklahoma, USA: Links between wastewater injection and the 2011 Mw 5.7 earthquake sequence. *Geology*, *41*(6), 699–702. https://doi.org/10.1130/G34045.1

Kilgore, B., N. M. Beeler, J. Lozos, and D. Oglesby (2017), Rock friction under variable normal stress, Journal of Geophysical Research: Solid Earth, 122, 7042–7075. https://doi.org/10.1002/2017JB014049.

Knopoff, L., & MacDonald, G. J. F. (1958). Attenuation of Small Amplitude Stress Waves in Solids. Reviews of Modern Physics, 30(4), 1178–1192. https://doi.org/10.1103/RevModPhys.30.1178

Langenbruch, C., Ellsworth, W. L., Woo, J.-U., & Wald, D. J. (2020). Value at Induced Risk: Injection-Induced Seismic Risk From Low-Probability, High-Impact Events. *Geophysical Research Letters*, *47*(2), e2019GL085878. https://doi.org/10.1029/2019GL085878

Lei, X., Wang, Z., & Su, J. (2019). The December 2018 ML 5.7 and January 2019 ML 5.3 Earthquakes in South Sichuan Basin Induced by Shale Gas Hydraulic Fracturing. *Seismological Research Letters*, *90*(3), 1099–1110. https://doi.org/10.1785/0220190029

Linker, M. F., & Dieterich, J. H. (1992). Effects of variable normal stress on rock friction: Observations and constitutive equations. *Journal of Geophysical Research Solid Earth*, *97*(B4), 4923–4940. https://doi.org/10.1029/92JB00017

Lockner, D. A., & Beeler, N. M. (1999). Premonitory slip and tidal triggering of earthquakes *Journal of Geophysical Research: Solid Earth*, *104*(B9), 20133–20151. https://doi.org/10.1029/1999JB900205

McGarr, A. (2014). Maximum magnitude earthquakes induced by fluid injection. *Journal of Geophysical Research: Solid Earth*, *119*(2), 1008–1019. https://doi.org/10.1002/2013JB010597

Nagata, K., Kilgore, B., Beeler, N., & Nakatani, M. (2014). High-frequency imaging of elastic contrast and contact area with implications for naturally observed changes in fault properties. *Journal of Geophysical Research: Solid Earth*, *119*(7), 5855–5875. https://doi.org/10.1002/2014JB011014

Nagata, K., Nakatani, M., & Yoshida, S. (2008). Monitoring frictional strength with acoustic wave transmission. *Geophysical Research Letters*, *35*(6), L06310. https://doi.org/10.1029/2007GL033146

Nagata, K., Nakatani, M., & Yoshida, S. (2012). A revised rate- and state-dependent friction law obtained by constraining constitutive and evolution laws separately with laboratory data. *Journal of Geophysical Research (Solid Earth)*, *117*, 2314. https://doi.org/10.1029/2011JB008818

Niemeijer, A. R., & Spiers, C. J. (2007). A microphysical model for strong velocity weakening in phyllosilicate-bearing fault gouges. *Journal of Geophysical Research: Solid Earth*, *112*(B10), B10405. https://doi.org/10.1029/2007JB005008

Noël, C., Giorgetti, C., Scuderi, M. M., Collettini, C., & Marone, C. (2023). The Effect of Shear Displacement and Wear on Fault Stability: Laboratory Constraints. Journal of Geophysical Research: Solid Earth, 128(4), e2022JB026191. https://doi.org/10.1029/2022JB026191

Noël, C., Pimienta, L., & Violay, M. (2019). Time-Dependent Deformations of Sandstone During Pore Fluid Pressure Oscillations: Implications for Natural and Induced Seismicity. Journal of Geophysical Research: Solid Earth, 124, 801–821. https://doi.org/10.1029/2018JB016546

Passelègue, F., X, Brantut, N., &Mitchell, T. M. (2018). Fault reactivationby fluid injection: Controls from stressstate and injection rate.Geophysical Research Letters,45, 12837–12846.https://doi.org/10.1029/2018GL080470

Noël, C., Passelègue, F. X., Giorgetti, C., & Violay, M. (2019). Fault Reactivation During Fluid Pressure Oscillations: Transition From Stable to Unstable Slip. Journal of Geophysical Research: Solid Earth, 124(11), 10940–10953. https://doi.org/10.1029/2019JB018517

Pearson, K., & Galton, F. (1997). VII. Note on regression and inheritance in the case of two parents. *Proceedings of the Royal Society of London*, *58*(347–352), 240–242. https://doi.org/10.1098/rspl.1895.0041

Perfettini, H., Schmittbuhl, J., Rice, J. R., & Cocco, M. (2001). Frictional response induced by time-dependent fluctuations of the normal loading. *Journal of Geophysical Research: Solid Earth*, *106*(B7), 13455–13472. https://doi.org/10.1029/2000JB900366

Pignalberi, F., Giorgetti, C., Noël, C., Marone, C., Collettini, C., & Scuderi, M. M. (2024). The effect of normal stress oscillations on fault slip behavior near the stability transition from stable to unstable motion. Journal of Geophysical Research: Solid Earth, 129, e2023JB027470. https://doi.org/10.1029/2023JB027470

Prakash, V. (1998). Frictional Response of Sliding Interfaces Subjected to Time Varying Normal Pressures. *Journal of Tribology*, *120*(1), 97–102. https://doi.org/10.1115/1.2834197

Rice, J. R. (2006). Heating and weakening of faults during earthquake slip. *Journal of Geophysical Research*, *111*(B5), B05311. https://doi.org/10.1029/2005JB004006

Rice, J. R., & Ruina, A. L. (1983). Stability of Steady Frictional Slipping. *Journal of Applied Mechanics*, *50*(2), 343–349. https://doi.org/10.1115/1.3167042

Richardson, E., & Marone, C. (1999). Effects of normal stress vibrations on frictional healing . *Journal of Geophysical Research: Solid Earth*, *104*(B12), 28859–28878. https://doi.org/10.1029/1999JB900320

Ruina, A. (1983). Slip instability and state variable friction laws. *Journal of Geophysical Research Solid Earth*, *88*(B12), 10359–10370. https://doi.org/10.1029/JB088iB12p10359

Scholz, C. H. (2018). The Mechanics of Earthquakes and Faulting. https://doi.org/10.1017/9781316681473

Schuster, A. (1997). On lunar and solar periodicities of earthquakes. *Proceedings of the Royal Society of London*, *61*(369-377), 455–465. https://doi.org/10.1098/rspl.1897.0060

Scott, D. R., Marone, C. J., & Sammis, C. G. (1994). The apparent friction of granular fault gouge in sheared layers. Journal of GeophysicalResearch, 99(B4), 7231–7246. https://doi.org/10.1029/93JB03361

Segall, P., & Lu, S. (2015). Injection-induced seismicity: Poroelastic and earthquake nucleation effects. *Journal of Geophysical Research: Solid Earth*, *120*(7), 5082–5103. https://doi.org/10.1002/2015JB012060

Shreedharan, S., Bolton, D. C., Rivière, J., & Marone, C. (2020). Preseismic Fault Creep and Elastic Wave Amplitude Precursors Scale With Lab Earthquake Magnitude for the Continuum of Tectonic Failure Modes. *Geophysical Research Letters*, *47*(8), e2020GL086986. https://doi.org/10.1029/2020GL086986

Shreedharan, S., Bolton, D. C., Rivière, J., & Marone, C. (2021). Competition between preslip and deviatoric stress modulates precursors for laboratory earthquakes. *Earth and Planetary Science Letters*, *553*, 116623. https://doi.org/10.1016/j.epsl.2020.116623

Shreedharan, S., Rivière, J., Bhattacharya, P., & Marone, C. (2019). Frictional State Evolution During Normal Stress Perturbations Probed With Ultrasonic Waves. *Journal of Geophysical Research: Solid Earth*, *124*(6), 5469–5491. https://doi.org/10.1029/2018JB016885

Sleep, N. H., & Blanpied, M. L. (1994). Ductile creep and compaction: A mechanism for transiently increasing fluid pressure in mostly sealed fault zones. *Pure and Applied Geophysics*, *143*(1), 9–40. https://doi.org/10.1007/BF00874322

Somfai, E., Roux, J.-N., Snoeijer, J. H., van Hecke, M., & van Saarloos, W. (2005). Elastic wave propagation in confined granular systems. *Physical Review E*, *72*(2), 021301. https://doi.org/10.1103/PhysRevE.72.021301

Spiers, C. J., S.De Meer, A. R. Niemeijer, and X. Zhang (2004), Kinetics of rock deformation by pressure solution and the role of thin aqueous films, in Physicochemistry of Water in Geological and Biological Systems, edited by S. Nakashima et al., pp. 129–158, Univ. Acad. Press, Inc., Tokyo.

Verdon, J. P. (2014). Significance for secure CO2 storage of earthquakes induced by fluid injection. *Environmental Research Letters*, *9*(6), 064022. https://doi.org/10.1088/1748-9326/9/6/064022

Vidal, V., Oliver, C., Lastakowski, H., Varas, G., & Géminard, J. C. (2019). Friction weakening by mechanical vibrations: A velocity-controlled process. *The European Physical Journal E*, *42*(7), 91. https://doi.org/10.1140/epje/i2019-11855-2

Yang, H., Zhou, P., Fang, N., Zhu, G., Xu, W., Su, J., Fanbao, M., & Chu, R. (2020). A Shallow Shock: The 25 February 2019 ML 4.9 Earthquake in the Weiyuan Shale Gas Field in Sichuan, China. *Seismological Research Letters*, *91*, 3182–3194. https://doi.org/10.1785/0220200202

Yoshioka, N., & Iwasa, K. (2006). A laboratory experiment to monitor the contact state of a fault by transmission waves. *Tectonophysics*, *413*(3), 221–238. https://doi.org/10.1016/j.tecto.2005.10.035

Yu, B., Yao, L., Ma, S., & Qin, W. (2023). Shear-induced distortion of clay minerals aids in dynamic weakening of shallow faults during earthquakes. *Earth and Planetary Science Letters*, *602*, 117971. https://doi.org/10.1016/j.epsl.2022.117971

Yu, B., Chen, J., Spiers, C. J., Ma, S., Zhang, M., Qi, W., Chen, H. (2024). Experimental data for the manuscript <Frictional Properties of Simulated Fault Gouges subject to Normal Stress Oscillation and Implications for Induced Seismicity> [Dataset]. Zenodo. https://zenodo.org/records/10472106

Yu, C., Ji, S., & Li, Q. (2016). Effects of porosity on seismic velocities, elastic moduli and Poisson's ratios of solid materials and rocks. *Journal of Rock Mechanics and Geotechnical Engineering*, *8*(1), 35–49. https://doi.org/10.1016/j.jrmge.2015.07.004

Zhang, H., Tong, H., Zhang, P., He, Y., Liu, Z., & Huang, Y. (2022). How can casing deformation be prevented during hydraulic fracturing of shale gas?—A case study of the Weiyuan area in Sichuan, China. Journal of Petroleum Science and Engineering, 221, 111251. https://doi.org/10.1016/j.petrol.2022.111251

Zhu, J. B., Kang, J. Q., Elsworth, D., Xie, H. P., Ju, Y., & Zhao, J. (2021). Controlling Induced Earthquake Magnitude by Cycled Fluid Injection, Geophysical Research Letters, 48, e2021GL092885. https://doi.org/10.1029/2021GL092885

[Journal of Geophysical Research: Solid Earth]

Supporting Information for

Frictional Properties of Simulated Fault Gouges subject to Normal Stress Oscillation and Implications for Induced Seismicity

Bowen Yu[1], Jianye Chen[1*], Christopher J. Spiers[1,2], Shengli Ma[1], Miao Zhang, Wenbo Qi and Hao Chen[1]

[1]State Key Laboratory of Earthquake Dynamics, Institute of Geology, China Earthquake Administration, Beijing, China.

[2]HPT Laboratory, Department of Earth Sciences, Utrecht University, Netherlands.

Contents of this file

Introduction

This document provides additional information regarding the sample composition, experimental procedure and details of the numerical simulation.

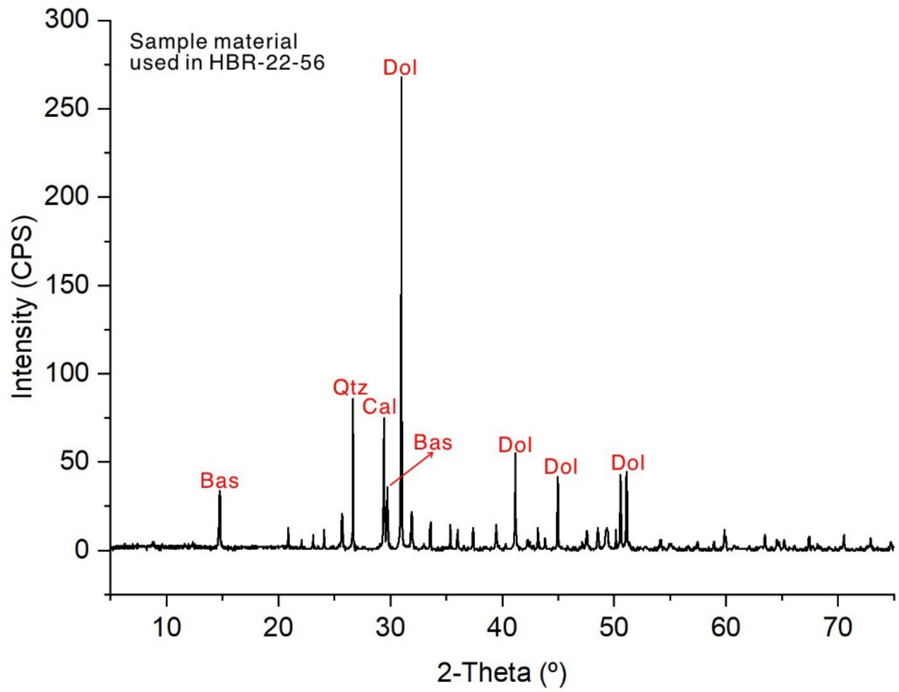

Figure S1. XRD test result for the gouge material, which was used to represent a slightly velocity-weakening fault gouge (SVW gouge). Dol: dolomite, Bas: bassanite, Cal: calcite, Qtz: quartz.

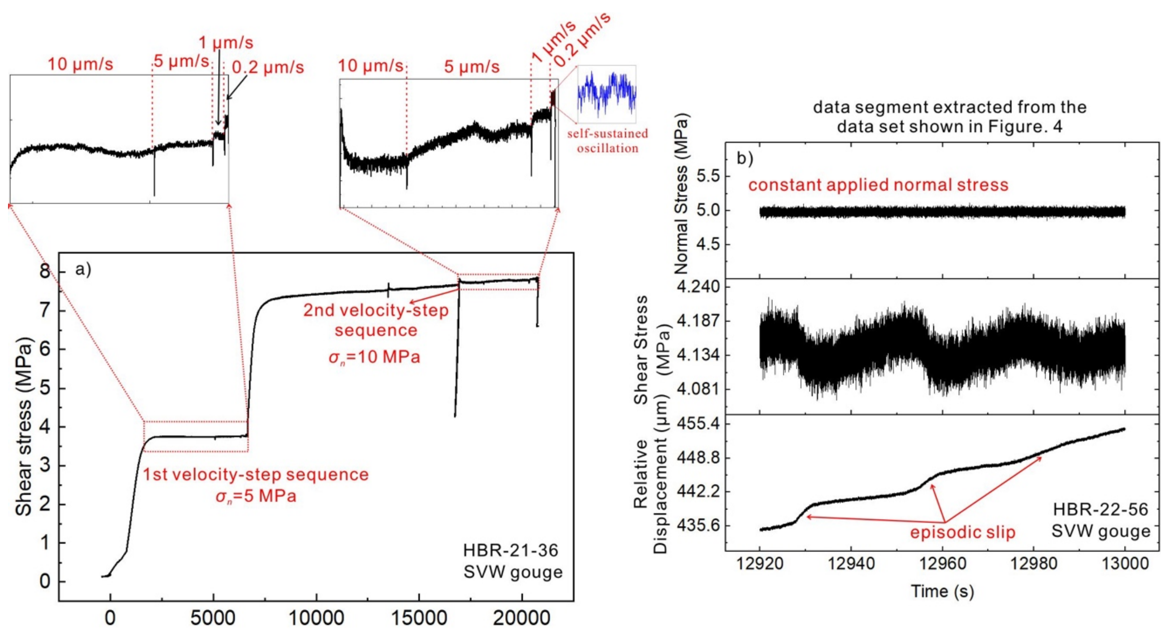

Figure S2. a) Results of velocity-step testing on the SVW gouge, performed at normal stresses σ_n of 5 MPa and then 10 MPa. The gouge showed self-sustained oscillation behavior under quasi-static shear loading and slightly velocity weakening behavior during velocity step testing. We performed the test shown in Fig. S2a separately and did not employ an LVDT to measure fault sliding displacement, so we cannot add this to Figure S2a. b) Self-sustained oscillation observed in this study; data was extracted from Figure 4 in the main text. In Figures 4 and S2b, the imposed normal stress and load-point velocity were constant at 5 MPa and 0.25 μm/s respectively.

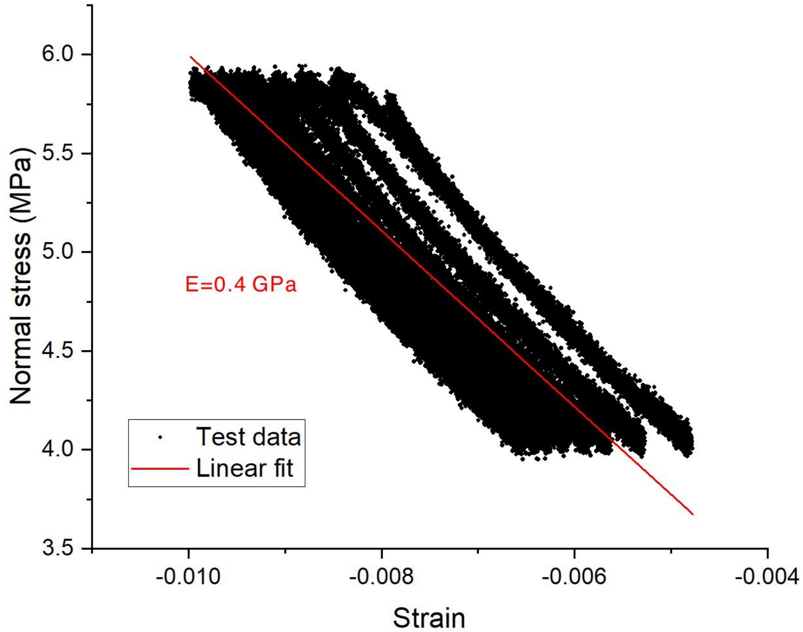

Figure S3. Relationship between average layer-normal strain and applied normal stress for two gouge layers tested in the double direct shear configuration employed in the present study. The data is derived from the normal load cycling test phase, applied before running shear experiment HBR-22-56 (Table 1 in the main text).

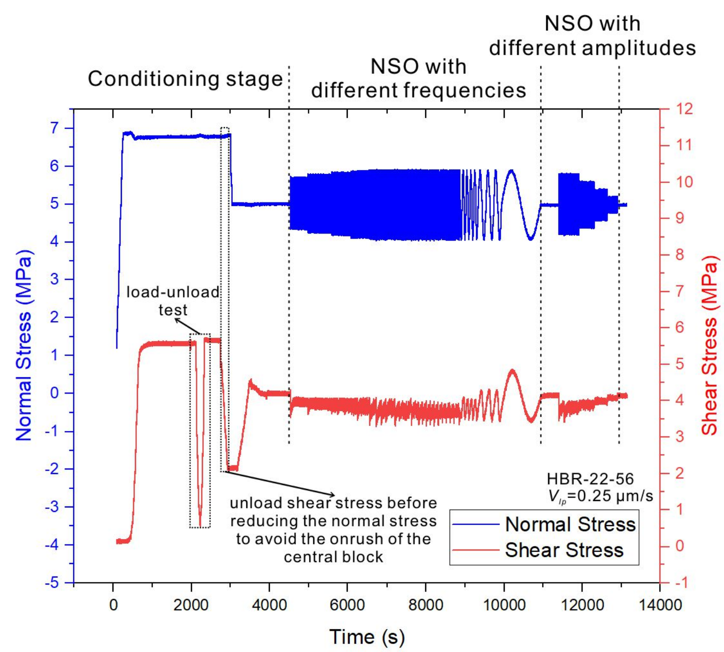

Figure S4. Typical results of a normal stress oscillation test performed during shear. Applied normal stress and measured shear stress are represented by the blue and red curves. We implemented two types of NSO in one experiment, namely Type I (5500 s–7000 s): NSO with different oscillation frequencies while the oscillation amplitude is kept constant; and Type II

(7000 s–7700 s): NSO with different oscillation amplitudes while oscillation frequency is kept constant.

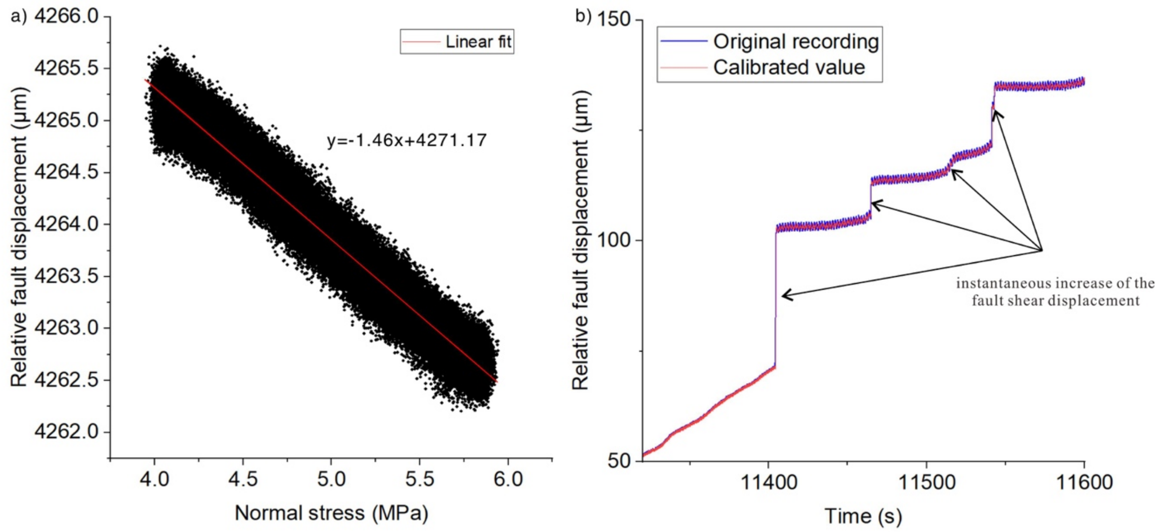

Figure S5. Calibration of the unexpected variation of fault shear displacement due to local distortion of the sample assembly. a) Relationship between applied normal stress and fault shear displacement recorded by LVDT. The data are derived from the normal load cycling test phase, performed before experiment HBR-22-56. According to the linear fit, a calibration factor of -1.46 was obtained. b) Comparison between original recording of fault shear displacement (blue) and corrected data after calibration (red). Given that the calibration does not have significant influence on the magnitude of the instantaneous increase of the fault shear displacement increase accompanied by the unstable slip events (the variable that we mainly focus on), the effects of sample distortion is thus ignored.

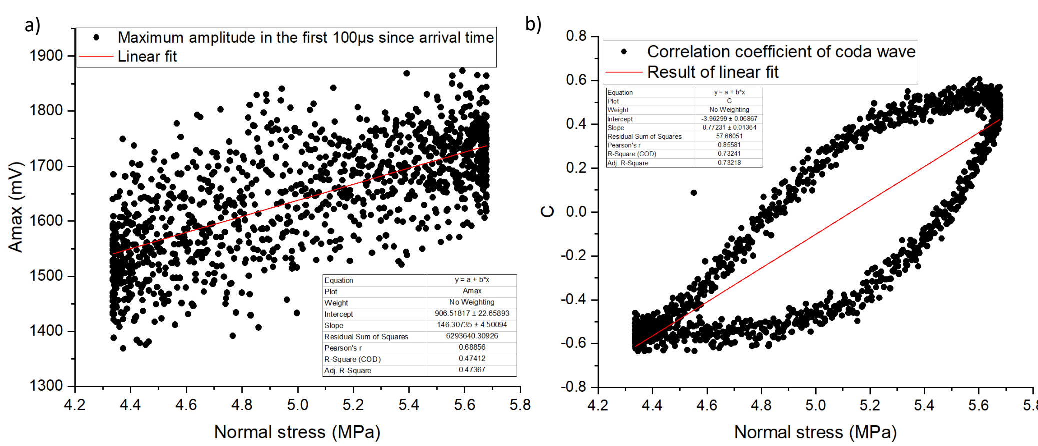

Figure S6. Linear functions used to subtract elastic effects caused by NSO. (a) and (b) display the functions used in calibrating the transmission coefficient and coda wave correlation coefficient, respectively. The maximum or A_{max} amplitude value is adopted here so that the time recorded in the ultrasonic dataset can be in agreement with that in the mechanical dataset. The data come from experiments conducted at NSO amplitude 20% and frequency 1Hz. We did not calibrate the wave velocity because it is not sensitive to unstable events occurring during NSO, due to the low pulse rate of the ultrasonic source. Note that the linear fit in Figure (b) only represents an estimate of the elastic component because the behavior is not fully elastic at 1 Hz as shown by the hysteresis.

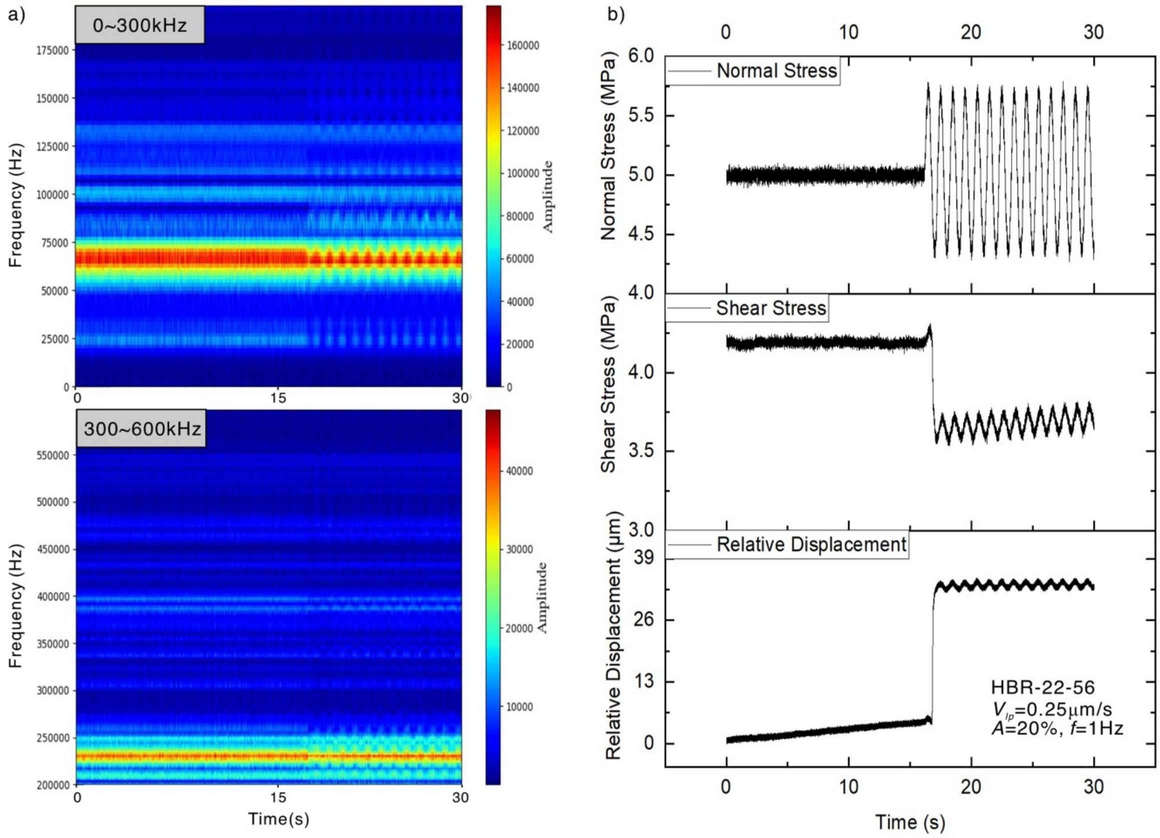

Figure S7. (a) Amplitude spectra of the received acoustic signal and (b) corresponding mechanical data.

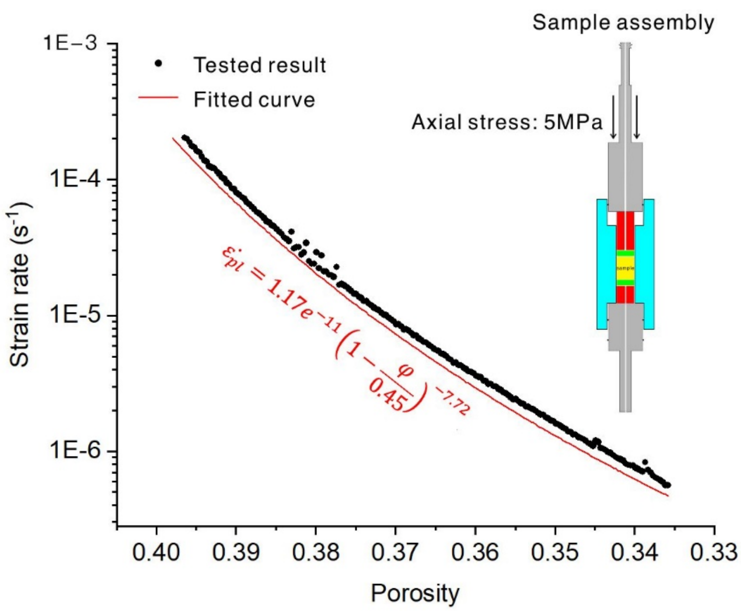

Figure S8. Relationship between porosity and compaction creep strain rate for SVW gouge, obtained in a uniaxial compaction test performed under room temperature and humidity conditions, with the axial stress kept constant at 5MPa. The inset figure shows the uniaxial compaction assembly, in which axial strain change is measured in terms of displacement of the top piston relative to the compaction vessel. Porosity was calculated following the analytical method reported by Zhang et al. (2010), where the density of rock framework is 2.77 g/cm^3, and the diameter, initial thickness and mass of the gouge sample are 10mm, 9.86mm and 1.2g, respectively. The fitting curve was obtained based on the function given in Eq. (17) in the main text.

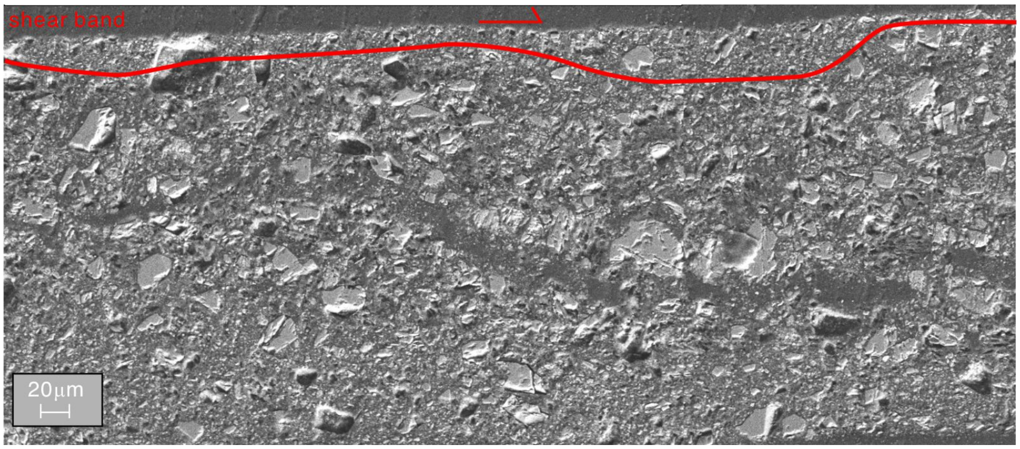

Figure S9. Microstructure of the SVW gouge collected after experiment HBR-22-56. Red arrow and red line indicate the shear sense and the shear band, respectively.

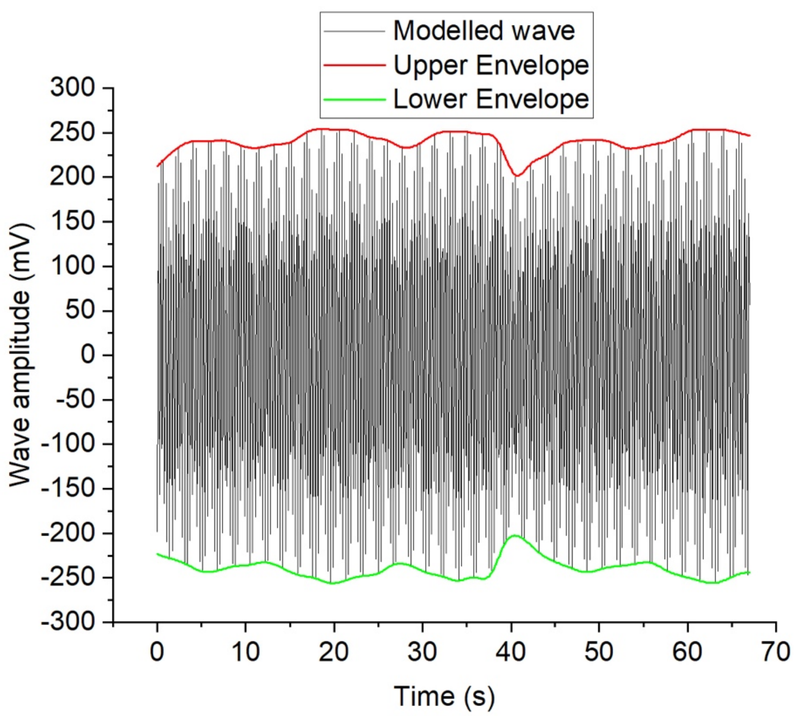

Figure S10. Modeled result of original waveforms. Red and green curves indicate upper and lower envelopes.

Time Scale	Expression	Theoretical Value	Reference
T_c	$T_c = D_c/V$	27.36 s	Characteristic evolution time. V=0.25e-6 m/s, D_c=6.84e-6 m, derived from the data of velocity-step test (from 5 to 1 m/s) shown in Fig. S2a.
$T_{critical}$	$T_{critical} = \frac{2\pi D_c \sqrt{\frac{a}{b-a}}}{V}$	362 s	Eq. (2) in the main text, which can be seen as the shortest recurrence time of any instabilities. V=0.25e-6 m/s, D_c=6.84e-6 m, a=0.007, b=0.00857, derived from the data of velocity-step test (from 5 to 1 m/s, σ_n=5 MPa) shown in Fig. S2a.
T_{pl}	$T_{pl} = \frac{1}{\dot{\varepsilon_{pl}}} = \frac{L_t}{V tan\psi}$	1.2e5 s	Time scale regarding the plastic flow. Derived from Eq. (5b) when considering $\dot{\varphi}^{sb} = 0$. Assuming V=0.25e-6 m/s, $tan\psi$ = 0.01, L_t=3e-4 m.
T_σ	/	1-1000 s	Period of the applied normal stress oscillation in experiment

Table S1. Three inherent time scales for frictional fault sliding (T_c, $T_{critical}$, and T_{pl}). T_σ refers to the period of the applied normal stress oscillation.

Parameter	Description	Value	Data Source and References
A_0	Amplitude of incident wave (mV)	1	Assumed here as we discuss about the normalized amplitude of transmitted elastic waves
ξ_{gran}	Attenuation factor of granite (m^{-1})	5e-4	A commonly acceptable value
ξ_{gouge}	Attenuation factor of gouge (m^{-1})	5e-4	
W_o	Width of outer granite of DDS configuration (m)	50e-3	Applied in experiments
W_i	Width of inner block of DDS configuration (m)	50e-3	
k	Wave number of incident wave	22.5	
ω	Corner frequency of incident wave (Hz)	$2\pi \cdot 0.1e6$	
d_{sb}	Average grain size of shear band (m)	0.63e-6	Estimated from microstructure
d_{bulk}	Average grain size of bulk gouge layer (m)	2e-5	
β	A factor that can transfer contact area to contact stiffness	7e14	(Nagata et al., 2014)

Table S2. Parameters utilized in the forward modeling of transmitted ultrasonic waves.

References

Nagata, K., Kilgore, B., Beeler, N., & Nakatani, M. (2014). High-frequency imaging of elastic contrast and contact area with implications for naturally observed changes in fault properties. Journal of Geophysical Research: Solid Earth, 119(7), 5855-5875. https://doi.org/10.1002/2014JB011014

Zhang, X., Spiers, C. J., & Peach, C. J. (2010). Compaction creep of wet granular calcite by pressure solution at 28°C to 150°C. Journal of Geophysical Research: Solid Earth, 115(B9). https://doi.org/10.1029/2008JB005853